JOURNAL OF PROPULSION AND POWER
Vol. 26, No. 4, July–August 2010

Particle-Based Plasma Simulations for an Ion Engine Discharge Chamber

Sudhakar Mahalingam*
Tech-X Corporation, Boulder, Colorado 80303
and
James A. Menart†
Wright State University, Dayton, Ohio 45435

DOI: 10.2514/1.45954

A particle-based model with a Monte Carlo collision model has been developed to study the plasma inside the discharge chamber of an ion engine. This model tracks five major particle types inside the discharge chamber in detail: xenon neutrals, singly charged xenon ions, doubly charged xenon ions, secondary electrons, and primary electrons. Both electric and magnetic field effects are included in the calculation of the charged particle's motion. The electric fields inside the discharge chamber are computed using a new approach. Also, detailed particle collision mechanisms are enabled. Validation of this computational model has been made on NASA's three-ring Solar Electric Propulsion Technology Application Readiness Program discharge chamber, at the 2.29 kW input power, 1.76 A beam current, and 1100 V beam voltage operating condition. Comparisons of numerical simulation results with experimental measurements are found to have good agreement. The computed ion beam current differs from experiments by 1% and the computed discharge current differs from experiments by 22%. The plasma ion production cost compares within 7% and the beam ion production cost compares within 16% of the experimental values. The overall computed thruster efficiency is found to differ from experiments by 11%. In addition, steady-state results are given for particle number density distributions, kinetic energy, particle energy loss mechanisms, and current density collected at the chamber walls.

Nomenclature

$\mathbf{B}$	=	magnetic field vector, tesla
$\mathbf{E}$	=	electric field vector, V m^{-1}
$\|e\|$	=	absolute electron charge, 1.6×10^{-19} C
F_B	=	beam flatness parameter
F_t	=	thrust reduction factor
I_A	=	anode ion current, A
I_B	=	beam ion current, A
I_B^+	=	beam ions current due to singly charged ions, A
I_B^{++}	=	beam ions current due to doubly charged ions, A
I_B^*	=	variant of beam ion current ($I_B^+ + 0.5 * I_B^{++}$), A
I_C	=	cathode ion current, A
I_D	=	discharge current, A
I_E	=	cathode emission current, A
I_P	=	total ion production current inside the discharge chamber, A
I_{SG}	=	screen grid ion current, A
I_{sp}	=	specific impulse, s
$jB+$	=	beam current density based on I_B^*, A/m^2
$jB++$	=	beam current density based on I_B, A/m^2
k_B	=	Boltzmann constant, 1.38065×10^{-23}
m_e	=	mass of an electron, 9.11×10^{-31} kg
m_i	=	mass of an ith-type particle, kg
m_{Xe}	=	mass of a xenon atom, kg
$\dot{m}_{\mathrm{cathode}}$	=	neutral flow rate through discharge chamber hollow cathode, kg s^{-1} or sccm
$\dot{m}_{\mathrm{main}}$	=	neutral flow rate through main plenum, kg s^{-1} or sccm
N_{cell}	=	number of computational cells
N_{cp}	=	number of computer particles
$N_{e,\mathrm{cell}}$	=	average number of computer electron particles per cell
$N_{\mathrm{iter,charge}}$	=	number of iterations for charge particles convergence
$N_{\mathrm{iter,Xe}}$	=	number of iterations for Xe convergence
N_{phys}	=	total number of physical particles
N_r	=	number of radial grid points
N_z	=	number of axial grid points
n	=	target particle density, m^{-3}
n_e	=	number density of electrons, m^{-3}
n_i	=	number density of ions, m^{-3}
$\dot{n}_{\mathrm{pe}}$	=	primary electron emission rate through hollow cathode, m^{-3} s^{-1}
$\dot{n}_{\mathrm{Xe,cathode}}$	=	neutral xenon volumetric flow rate through hollow cathode, m^{-3} s^{-1}
$\dot{n}_{\mathrm{Xe,main}}$	=	neutral xenon volumetric flow rate through main plenum, m^{-3} s^{-1}
P	=	probability
P_{IN}	=	input power, W or kW
q_i	=	charge of an ith-type particle, C
T	=	calculated thrust, N or mN
T_{actual}	=	actual thrust generated, N or mN
T_{avg}	=	average energy of plasma particles, eV
T_{cathode}	=	cathode wall temperature, eV or K
T_e	=	electron temperature, eV or K
T_{main}	=	discharge chamber wall temperature at main plenum, eV or K
$T_{\mathrm{pe,init}}$	=	primary electron initial energy at the hollow cathode, eV
T_0	=	neutral xenon initial energy, eV
t	=	time, s
t_s	=	wall sheath thickness, m
V_{ACC}	=	accelerator grid voltage, V
V_B	=	beam voltage, V

Presented as Paper 2008-4733 at the 44th AIAA/ASME/SAE/ASEE Joint Propulsion Conference and Exhibit, Hartford, CT, 21–23 July 2008; received 11 June 2009; revision received 8 December 2009; accepted for publication 6 February 2010.

*Research Scientist, 5621 Arapahoe Avenue, Suite A. Member AIAA.
†Professor, Mechanical and Materials Engineering Department, 209 Russ Engineering Center. Associate Fellow AIAA.

V_{bulk} = bulk plasma potential, V
V_D = discharge voltage, V
V_C = hollow cathode voltage, V
$V_{c_{\text{tip}}}$ = cathode tip volume, m^3
V_{main} = main plenum neutral source volume, m^3
v_t = thermal speed of electron, $m\,s^{-1}$
$\mathbf{v}_i$ = particle velocity vector, $m\,s^{-1}$
$|\mathbf{v}_{\text{inc},e}|$ = magnitude of incident electron velocity, $m\,s^{-1}$
$\mathbf{v}_{\text{pe}}$ = primary electron velocity vector, $m\,s^{-1}$
$\mathbf{v}_{\text{Xe,cathode}}$ = neutral xenon velocity vector through hollow cathode, $m\,s^{-1}$
$\mathbf{v}_{\text{Xe,main}}$ = neutral xenon velocity vector through main plenum, $m\,s^{-1}$
W_{macro} = computer or macroparticle weight
Xe = neutral xenon
Xe^+ = singly charged xenon ion
Xe^{++} = doubly charged xenon ion
$\mathbf{x}_i$ = particle position vector, m
Z = ion charge state

Greek Symbols

α = correction factor due to the double ion content in the beam current
α_r^{ee++} = three-body recombination coefficient for doubly charged ions, $m^6\,s^{-1}$
α_r^{ee+} = three-body recombination coefficient for singly charged ions, $m^6\,s^{-1}$
Δt_e = time step size for electron, s
Δt_{ion} = time step size for ion, s
Δt_{Xe} = time step size for neutral xenon, s
η_{prop} = discharge chamber propellant utilization efficiency, %
η_t = overall thruster efficiency, %
ϵ_B = beam ion production cost, eV/ion or W/A
ϵ_{ionz} = ionization potential, eV
ϵ_p = plasma ion production cost, eV/ion or W/A
ε_0 = permittivity of free space constant, $8.854 \times 10^{-12}\ F\,m^{-1}$
ε_a = artificial plasma permittivity, $F\,m^{-1}$
γ_i = ion-induced secondary electron emission coefficient
λ_D = Debye length, m
ω_{pe} = plasma frequency, $rad\,s^{-1}$
ϕ = electric potential, V
ϕ_{dy} = dynamic electric potential, V
ϕ_{st} = static electric potential, V
ϕ_{wf} = work function of metal surface, eV
φ_{ion} = screen grid transparency to ions
φ_0 = screen grid transparency to neutrals
ρ = charge density, $C\,m^{-3}$
$\sigma(t)$ = collision cross section, m^2
$\sigma_{ee++,r}$ = three-body recombination cross section, m^2
Δ = two-dimensional characteristic grid spacing, m
ζ = scale factor

I. Introduction

COMPUTATIONAL modeling of an ion engine discharge plasma can provide many significant insights into the developments of the next-generation ion engines. The life limiting mechanisms of an ion engine such as the erosion of the hollow cathode and the grid optics can be better understood if we know the plasma near these locations. The computational model being discussed in this paper simulates the entire discharge chamber plasma and provides insight into the physical characteristics of the discharge plasma. Ion engine discharge chamber computational models that have been developed in the past either ignore many of the particle types in the discharge chamber or model one or two of the particle types using a particle-tracking technique and model the rest of the particles using a diffusion approach, i.e., based on fluid assumptions [1–5]. The advantage of the diffusion based plasma simulations is that they reach convergence much quicker than the particle-based plasma simulations [6,7]. The disadvantages of diffusion based models are that they make many approximations to consider the electron and ion distributions in the discharge chamber, particle energy values, collision rates and simplified quasi-neutrality assumptions. Our present model employs a particle-tracking approach for all of the major particles inside the discharge chamber. By employing a particle-based approach, the discharge chamber computational model minimizes the number of assumptions made on the distribution functions for electrons, ions and the collision rates inside the discharge chamber.

A full scale computational model such as a particle-in-cell (PIC) technique [8,9] is an ideal choice for modeling the physics of the plasma in an ion engine discharge chamber, except for the fact that a PIC simulation is an extremely time intensive calculation [6,7]. Our earlier PIC computational models consider most of the physics occurring inside the discharge chamber in a detailed manner by individually tracking three major charged particles (primary electrons, secondary electrons, and ions) in the presence of electric and magnetic fields. These models solved for the entire dynamic electric fields caused by the charge particle distributions. The neutral particles were assumed to be uniformly distributed throughout the discharge chamber. Some early results for a small 10-cm diameter, three-ring discharge chamber using this PIC technique that attempted to determine the entire dynamic electric field were presented. The total particle results indicated that the PIC simulation needed to be run much longer than is reasonably feasible to reach a steady state condition. As stated by Taccogna et al. [10], steady state solutions for the typical electric thruster using a PIC technique can be expected after a few hundred microseconds. Using 16 processors in a parallel PIC simulation took 20 days of computational run time to reach a time level of 5 μs [7]. This long computational time to reach 5 μs indicates that years are required to reach a steady state condition. Hence a full PIC simulation that attempts to model the entire dynamic electric field effect in a detailed manner is impractical at the present time. This is even true when using the benefits of parallel processing. Previously, in our first attempt at a PIC approach to modeling a discharge chamber [11], we proposed no updating of the electric fields inside the discharge chamber based on charged particle distributions. The electric fields were considered by supplying an input electric field which uses experimental plasma potential measurements made inside the discharge chamber. This assumed the electric field was considered to include the effects of the charged particle distribution inside the discharge chamber. However, this model was found to give large charge imbalance inside the discharge chamber. This could not be avoided as no charge separation effects were included in the tracking of charged particles inside the discharge chamber.

A new approach has been developed in this work that allows the electric field effects on the charged particles along with solving the dynamic electric field based on the charge particle distributions. This approach helps avoid accumulation of negatively charged particles inside the discharge chamber as observed in our previous simulations [11]. An artificially increased plasma permittivity value is considered in this new dynamic electric field solver. This allows the possibility of performing self-consistent particle-in-cell Monte Carlo Collision (PIC-MCC) simulations on the ion engine discharge chamber. A similar approach was used by Szabo [12] in his hall thruster PIC-MCC simulations. Our approach differs from Szabo's computational model in the following respects:

1) Szabo does not include any input electric field information obtained from experiments.

2) His computational domain is relatively small compared with our ion engine discharge chamber computational domain.

3) He adopted an artificial mass ratio for heavy particles while our model tracks heavy particles with their actual mass values. Further details of our dynamic electric field solver are given in Sec. II.

Our present model individually tracks four charge particle types inside the discharge chamber: primary electrons, secondary electrons, singly charged positive xenon ions (Xe^+), and doubly

charged positive xenon ions (Xe^{++}). The model also tracks the neutral xenon atoms (Xe). Sec. II presents the mathematical model used for solving the static and dynamic fields inside the discharge chamber along with the particle tracking. Sec. III presents the numerical techniques and the simulation sequence followed in the computational model. In Sec. IV, steady state results for the three-ring NASA Solar Electric Propulsion Technology Application Readiness Program (NSTAR) discharge chamber at the TH-15 operating condition are given. Comparisons of steady state numerical results are made with experimental measurements. The particle distribution results, particle energy loss mechanisms, and current density collected at the walls are also presented.

II. Mathematical Model

A schematic of the computational domain considered in this work is given in Fig. 1. This computational domain includes the discharge chamber cavity, the cathode exit, the cathode-keeper walls, the chamber walls, the screen grid, and the magnetic circuit. The static magnetic field inside the discharge chamber is created by permanent magnets. These magnets are located on the outside surface of the discharge chamber walls and are not shown in Fig. 1. In this work, the following discharge chamber regions are not included: the inside of the cathode, the region between the keeper and the cathode, and the region downstream of the grid optics. The boundaries of the computational domain are drawn along the inside walls of these devices. This domain is chosen to focus the computational modeling effort on the plasma inside the ion engine discharge chamber. In the future this modeling work can be extended to include other regions so that a comprehensive tool will be available for modeling the entire ion engine.

Different features of the mathematical model such as 1) static magnetic and static electric fields, 2) dynamic electric fields, 3) particle tracking, 4) particle collisions, and 5) particle boundary conditions are presented below.

A. Static Fields

In an ion engine discharge chamber the electric fields are generated by the static electric potentials applied to the chamber boundaries and from the charge particle distributions. Using superposition principles [13], the electric potentials generated by each of these components can be modeled independently. Finally the electric potential results from each of these components can be added together to determine the total electric field. Thus the electric potential, ϕ, is given by

$$\phi = \phi_{st} + \phi_{dy} \tag{1}$$

In this work the static electric potentials inside the discharge chamber are modeled as shown in Fig. 2. This figure essentially shows three regions. The dark region next to the cathode comes from experimental measurements. The white region is the bulk of the discharge chamber volume and is labeled the bulk plasma. This region is essentially at the plasma potential. The third region is a small strip next to the walls that is called the sheath. The sheath region is where the electrical potential quickly changes from the bulk plasma potential to the wall potential. The electric potential shown in Fig. 2 is treated as the static portion of the total electric field determined by this model.

It should be recognized that the fields shown in Fig. 2 are an approximation of the fields that would actually exist in a discharge chamber with a plasma. That means they include the effects of the wall potentials and the effects of charged particles. Technically the static fields are only supposed to include the effects of the wall potentials. For our model it is beneficial to include particle effects into the static field. It is reasonable to call the field in Fig. 2 a static field because it does not change throughout the computation. This assumption provides a reasonable approximation of electric field effects on gross particle motions. To alleviate one of the major problems caused by this assumption, charge imbalance, dynamic electric fields are still calculated.

In addition to the electric potentials throughout the volume of the discharge chamber, all anode-biased discharge chamber walls are maintained at the discharge voltage potential. This includes the upstream wall of the discharge chamber where the cathode is located, the slanted wall, the side wall, and the flange to which the grids are attached. The screen grid is maintained at 0 V relative to discharge cathode common. The cathode-keeper assembly is modeled as an enclosed box in which the cathode surface is maintained at the cathode-keeper potential ($\sim$5 V) relative to discharge cathode common. The cathode source tip area, the region where the primary electrons are produced, is maintained at an electric potential as measured in experiments [14].

The magnetic field produced by the current flow in the discharge chamber is small compared with that produced by the permanent magnets located on the discharge chamber walls. Neglecting the small fields produced by the moving charges allows the magnetic field to be determined independently of the particle simulation. For the two-dimensional, axisymmetric discharge chamber, the static magnetic field produced by the permanent magnets is obtained by solving the magnetostatic part of Maxwell's equations.

B. Dynamic Electric Fields

Poisson's equation is used to deal with the electrical potential ϕ_{dy} and can be written as

$$\nabla \cdot (\varepsilon_0 \nabla \phi_{dy}) = -\rho \tag{2}$$

where

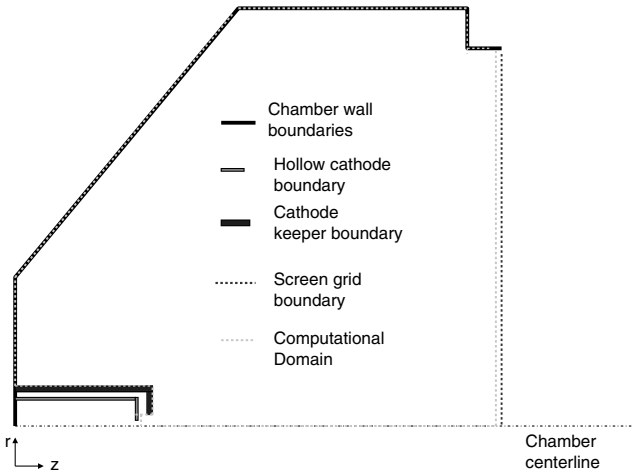

Fig. 1 Schematic of the computational domain considered in the PIC-MCC simulation.

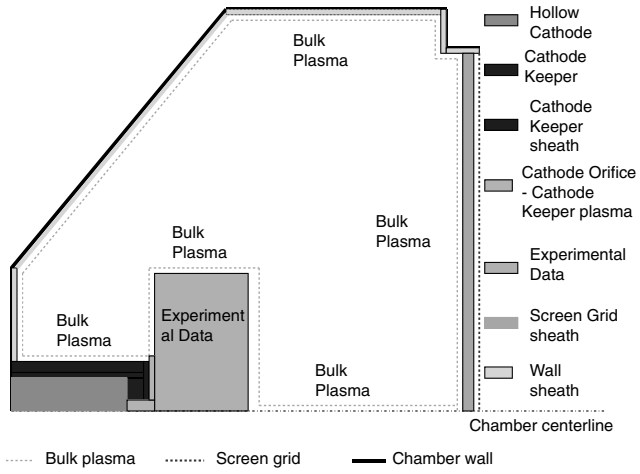

Fig. 2 Different static electric field regions considered in the PIC-MCC simulation.

$$\rho = |e|(n_i - n_e) \tag{3}$$

To solve Eq. (2) in a reasonable amount of computational time an approximation needs to be implemented. The approximation that is implemented in the solution of Eq. (2) is that the value of ε_0 is artificially increased to a larger value. This was done in a PIC simulation done for Hall thrusters by Szabo [12]. If this is not done a fine grid spacing and a small time step have to be used. These numerical parameters have to be made so small as to render computational times on the order of years. When ε_0 is made significantly large the effect of the dynamic electric potentials on the total potentials in the discharge chamber is relatively small. This is fine because the static field assumption made above includes the effects of charged particles. Thus the electric potential does not need to be altered extensively. The primary reason for solving the dynamic electric field equation is to allow charge neutrality to be obtained. If the dynamic electric fields are not computed, a large mismatch in the number of ions and the number of electrons in the discharge chamber arises [11]. This is physically unrealistic and this technique avoids this problem. Using the artificial plasma permittivity, $\varepsilon_a = \zeta\varepsilon_0$, in Eq. (2) gives

$$\nabla \cdot (\varepsilon_a \nabla \phi_{\mathrm{dy}}) = \nabla \cdot (\zeta\varepsilon_0 \nabla \phi_{\mathrm{dy}}) = -\rho \tag{4}$$

Here ζ is the scale factor use to get the artificial permittivity value. There are three criteria for our choice of artificial permittivity for simulations:

1) It needs to predict the microscopic electric fields such that a charge balance is maintained over the bulk of the discharge chamber.

2) The permittivity cannot be so small as to greatly alter the input electric potentials.

3) The permittivity must be large enough to allow for a computational cell size that makes the computations doable in three months as opposed to three years.

There are a range of permittivity values that will work as long as we keep the cell size smaller than the Debye length. The smallest grid spacing needs to resolve the smallest plasma Debye length in the discharge chamber. More details of how ζ and ε_a values are obtained for NSTAR discharge chamber simulation are presented in Sec. III.

Boundary conditions are also required to obtain a solution to Eq. (4). Since the potentials applied to the wall boundaries of the discharge chamber when it is in operation are taken care of by the static electric field model, the dynamic electric field model has these potentials set to a value of zero.

Lastly using the principle of superposition, the electric potentials are obtained by adding dynamic electric potential values to the static electric potential values as shown in Eq. (1). Once the total electric potential is determined the electric field, **E**, is obtained from

$$\mathbf{E} = -\nabla\phi \tag{5}$$

C. Particle Tracking

The Newton–Lorentz equation of motion is used to track the plasma particles in the electric and magnetic fields. This equation of motion is

$$m_i \frac{\mathrm{d}\mathbf{v}_i}{\mathrm{d}t} = q_i[\mathbf{E} + \mathbf{v}_i \times \mathbf{B}] \tag{6}$$

where

$$\frac{\mathrm{d}\mathbf{x}_i}{\mathrm{d}t} = \mathbf{v}_i \tag{7}$$

The electric field, **E**, and magnetic field, **B**, values at the particle locations are obtained by bilinear interpolation based on the field values at the surrounding grid nodes. The particle velocity and position are updated every time step from the time the particle is produced until it gets absorbed at one of the boundaries.

In this work, the electrons inside the discharge chamber are broken into two groups: primary and secondary electrons. Primary electrons are the high energy electrons that are emitted from the hollow cathode, while the low energy secondary electrons are produced from the ionizing collisions of electrons with Xe and Xe^+ inside the discharge chamber. Primary electrons that have slowed below a certain velocity after inelastic collisions with neutrals and ions are also included with the secondary electrons. This grouping helps to understand the behaviors of high energy and low energy electrons inside the discharge chamber. In this work we shift a primary electron into a secondary electron type when the primary electron has undergone an inelastic collision with a heavy particle and its energy goes below 4 eV. This modification is done to keep only high energy electrons in the primary electron group. There may be a few secondary electrons that obtain energies like primary electrons; however we do not move these secondary electrons into the primary electron group. The number of high energy secondary electrons is small.

In our early particle-based discharge chamber models [7], we assumed that the neutrals were distributed uniformly throughout the discharge chamber. Using this assumption in our simulations indicated that the neutrals were continually being depleted inside the discharge chamber. The problem is that this assumption only allows steady state solutions if the number of neutrals ionized is small relative to the number of neutrals present. This is not the case along the centerline of an ion engine. To maintain proper conservation of neutrals and to understand the neutral distribution inside the discharge chamber, we now track neutrals inside the discharge chamber. The neutrals are modeled using the same particle-tracking approach as the charged particles. Similarly we have enabled the tracking of Xe^{++}, as there is an interest in knowing the percentage of double ions present and their spatial distribution inside the discharge chamber. The double ion results are important since they will allow researchers to predict the lifetime issues of discharge chamber components.

Because of the high mass ratio of the heavy particles compared with the electrons ($\sim 2.4 \times 10^5$), the neutrals and the ions always move at a much slower speeds compared with the electrons. To handle this discrepancy in speeds a subcycling procedure is adopted for the heavy particles to minimize the computational run time. If the subcycling is set to 500, the heavy particles are advanced once for every 500 time steps that the electrons are advanced.

After advancing the particles, the particle number density distributions for the entire discharge chamber are computed for each particle type. This density calculation is used in the particle collision routines to handle the collisions of electrons, ions, and neutrals.

D. Particle Collisions

Table 1 shows the different types of particle collisions considered in this work. Monte-Carlo collision (MCC) techniques are used to handle the particle-particle interactions. Table 1 also contains the references for the collision cross-section data for each collision type that has been used in this work. It should be noted that elastic collisions between charged particles are handled by the dynamic electric field solution and are not included in Table 1.

In an electron-neutral ionization collision event, the incident electron loses the ionization threshold energy (12.1 eV) and gets

Table 1 Particle collisions considered in this PIC-MCC model

e–Xe	e–Xe^+	e–Xe^{++}	Xe^+–Xe	Xe^{++}–Xe
Elastic [15]	Excitation [16,17]	Excitation [16,17]	Elastic [18]	CEX [18]
Excitation [15]	Ionization [19]	Three-body recombination [20]	CEX [18]	——
Ionization [21]	Three-body recombination [20]	——	——	——

scattered. In the event of an elastic collision with a neutral, the electron does not lose its energy, but only gets scattered. In an excitation collision event, the electron loses the excitation threshold energy of 8.35 eV and gets scattered. In this model the excited states of neutrals are not maintained. It is assumed that this excitation energy is immediately radiated to the walls of the discharge chamber.

Inelastic electron-ion collisions such as excitation, ionization, and three-body recombination processes are included in the present model. From a literature survey, it was found that the electron-impact excitation cross-section data for both Xe^+ and Xe^{++} is sparse to nonexistant. For this reason the following approximations are made. A swarm analysis by Strinic et al. [16] provides cross-section data on electron-impact excitation collisions for the higher excitation levels of Xe^+. For the plasma in the discharge chamber the most excitation collisions occur from the ground level of the ion. Since no excitation cross-section data for ground level excitation of Xe^+ could be found, we have approximated the ground level excitation cross section to be the same as the upper level excitation results of the swarm analysis of Strinic et al. [16]. The threshold energy for the Xe^+ excitation collision is estimated using information available from the National Institute of Standards and Technology (NIST) Atomic Spectra Database [17,22]. There are many possible excitation transitions for Xe^+ from the ground state, we only look at one transition. This ground to excited level transition uses an average energy level value for the upper state of the transition of 14.8 eV. The same procedure is followed for determining the excitation energy for the electron-impact excitation collisions of Xe^{++}. Using the NIST Atomic Spectra Database [17,22], we approximate the excitation energy for an electron to excite Xe^{++} to be 19.1 eV. Also, since we could not find information for the excitation cross section of Xe^{++}, we have used the Xe^+ excitation cross-section data for Xe^{++} excitation collisions. Our physical parametric studies [23] indicated that the percentage of electron-impact Xe ion excitation processes happening inside the discharge chamber are relatively small. Hence these simplified cross-section assumptions did not affect the discharge plasma results significantly. In future work, we will improve this cross section data based on real experiments, if they become available.

In an electron-impact ionization collision of Xe^+, the incident electron loses the ionization threshold energy of 21.2 eV to produce a Xe^{++} particle and a secondary electron. The electron-impact ionization collisions of Xe^{++} are neglected in the model since the ionization threshold energy for these collisions are much larger than the applied discharge voltage.

Also included in this model are three-body electron-ion recombination processes. These inelastic collision processes [24] happen more frequently in high density plasmas with electron temperatures in the range of 1–2 eV, but they also occur in the ion engine discharge chamber plasma. The following recombination reactions are used in this model:

$$e + e + Xe^+ \longrightarrow Xe + e \tag{8}$$

$$e + e + Xe^{++} \longrightarrow Xe^+ + e \tag{9}$$

The three-body electron-ion recombination rate coefficient for Xe^{++} is given by

$$\alpha_r^{ee++} = 9 \times 10^{-39} T_e^{-9/2}\ \mathrm{m^6/s} \tag{10}$$

where T_e is the incident electron temperature in eV. From the literature search no recombination data could be found for xenon ions. In [20], the above recombination rate coefficient is used for the recombination of doubly charged aluminum ions. The same equation is used for the recombination rate for Xe^{++} ions. To obtain the Xe^{++} recombination cross section, $\sigma_{ee++,r}$, value the above equation needs to be divided by the electron number density and by the incident electron speed. It is given by

$$\sigma_{ee++,r} = \frac{\alpha_r^{ee++}}{n_e |\mathbf{v}_{\mathrm{inc},e}|} \tag{11}$$

Since the recombination process has a strong dependence on the ion charge state, Z, the three-body electron-ion recombination rate coefficient for the Xe^+ is estimated to be

$$\alpha_r^{ee+} = \frac{\alpha_r^{ee++}}{Z^3} \tag{12}$$

Both elastic and charge-exchange-type collisions are considered for the ion-neutral interactions. In an elastic collision, the ion will not lose its energy but will only get scattered. In a charge-exchange collision, the colliding ion becomes a neutral and the neutral becomes an ion.

E. Particle Boundary Conditions

The high energy primary electrons are emitted from the hollow cathode which is generally placed near the back wall of the discharge chamber on the centerline. Inside the hollow cathode tube, electrons are emitted by heating a low work function emitting material to a high temperature. The physical phenomena occurring inside the hollow cathode is very complex [25] and not included in this work. For this reason, electrons being emitted from the hollow cathode are taken as a boundary condition. This study uses a small electron source located at the exit from the hollow cathode to get primary electrons into the discharge chamber. The rate of electrons, $\dot{n}_{\mathrm{pe}}$, produced is based on the emission current from the cathode, I_E, and the volume of the cathode tip, $V_{c_{\mathrm{tip}}}$, chosen for plasma generation. The rate of plasma production is

$$\dot{n}_{\mathrm{pe}} = \frac{I_E}{|e| V_{c_{\mathrm{tip}}}} \tag{13}$$

Here the emission current, I_E, is calculated based on the current balance equation for the discharge chamber. It is given by

$$I_E = I_D - (I_{\mathrm{SG}} + I_C) \tag{14}$$

The speed at which the primary electrons are leaving the cathode tip is based on the electron temperature measured at the cathode tip location. The speed of the mono-energetic primary electrons, $|\mathbf{v}_{\mathrm{pe}}|$, is

$$\mathbf{v}_{\mathrm{pe}} = \sqrt{\frac{2|e|T_e}{m_e}} \tag{15}$$

where T_e is the electron temperature in eV. The flow path of primary electrons that leave the cathode source is taken as a stream directed towards the screen grid with a 15 ° half angle divergence [26]. In the actual hollow cathode arrangement the cathode orifice is a chamfered hole through which the electrons leave into the bulk discharge chamber plasma.

Neutrals are supplied to the discharge chamber through multiple orifices in the main plenum in the thruster, but due to symmetry are modeled as a single orifice in the model. Neutrals are also supplied through the hollow cathode. Both neutral sources are modeled as volumetric sources where the rate is based on the respective flow rates. The source rate of neutrals, $\dot{n}_{\mathrm{Xe,cathode}}$, through the hollow cathode is determined using

$$\dot{n}_{\mathrm{Xe,cathode}} = \frac{\dot{m}_{\mathrm{cathode}}}{m_{\mathrm{Xe}} V_{c_{\mathrm{tip}}}} \tag{16}$$

Similarly the main neutral source rate, $\dot{n}_{\mathrm{Xe,main}}$, is determined using

$$\dot{n}_{\mathrm{Xe,main}} = \frac{\dot{m}_{\mathrm{main}}}{m_{\mathrm{Xe}} V_{\mathrm{main}}} \tag{17}$$

where V_{main} is the main feed computational source volume.

The neutral's speed at the source is determined using the wall temperature measured at the emission locations. The neutral speed at the cathode source, $|\mathbf{v}_{\mathrm{Xe,cathode}}|$, is determined using

$$\mathbf{v}_{\mathrm{Xe,cathode}} = \sqrt{\frac{2|e|T_{\mathrm{cathode}}}{m_{\mathrm{Xe}}}} \tag{18}$$

where T_{cathode} is the wall temperature observed at the cathode orifice plate in eV. Similarly the neutral speed at the main feed location, $|\mathbf{v}_{\mathrm{Xe,main}}|$, is determined using

$$\mathbf{v}_{\mathrm{Xe,main}} = \sqrt{\frac{2|e|T_{\mathrm{main}}}{m_{\mathrm{Xe}}}} \tag{19}$$

where T_{main} is the wall temperature observed at the main feed locations given in eV. The flow path of neutrals exiting the hollow cathode are modeled in a similar fashion to the emission of primary electrons from the cathode. The neutral flow path from the main source is based on its location inside the discharge chamber.

All anode-biased discharge chamber walls absorb both electrons and ions that hit them. Whenever an ion hits a discharge chamber wall, it recombines with an electron at the wall and becomes a neutral. This neutral is reflected back into the discharge chamber. An additional event that may occur when an ion hits an anode-biased wall is secondary emission. When an ion hits an anode-biased wall there is a chance that an electron will be released from the wall surface to behave as a free electron in the computational domain. Whether this happens is determined by the secondary electron emission coefficient. The empirical formula for the secondary electron emission coefficient, γ_i, is obtained using [27]

$$\gamma_i = 0.016(\epsilon_{\mathrm{ionz}} - \phi_{\mathrm{wf}}) \tag{20}$$

where ϵ_{ionz} is the ionization potential given in eV and ϕ_{wf} is the work function necessary to extract an electron from a metal surface. The γ_i relation given above is independent of incident ion energies up to 1 keV [27], but it depends on the work function of the metal surface and the ionization potential. Whether a secondary electron is produced when an ion hits the wall is based on the γ_i value. This γ_i value is compared with a random number to determine whether secondary electron emission occurs.

Cathode biased walls absorb the ions that hit them and reflect the electrons that hit them. The cathode biased screen grid is set to have a transparency value for both ions and neutrals. The neutrals get reflected back into the discharge chamber if they hit any chamber or cathode wall. The reflection of neutrals from the walls is taken as being diffuse. This diffuse reflection randomizes the neutral's flow path in the discharge chamber. At the symmetry boundary condition (i.e., along the centerline of the discharge chamber) all particles are reflected in a specular manner.

III. Solution of Mathematical Model

Figure 3 shows a flow chart of the computing sequence used by the PIC-MCC simulation used in this work. In this flow chart the PIC-MCC simulation is divided into two pieces: a static piece and a dynamic piece. The dynamic piece of this algorithm deals with calculations that depend on the position of the particles in the discharge chamber. The static piece of the algorithm deals with input, boundary conditions, the computational mesh, the static magnetic field, and the static electric field. All computations done in the static portion of the algorithm are independent of the particle locations determined in the dynamic portion of the algorithm.

Two computational tools, MAXWELL-2D [28] and OOPIC [29,30], are used for solving the mathematical model presented in this work. MAXWELL-2D, a computer program developed by the ANSOFT Corporation, is used to model the magnetic field inside the discharge chamber. The discharge chamber wall locations, the wall material, magnet locations, and properties of the magnets are provided as input to MAXWELL-2D. MAXWELL-2D solves the magnetostatic field equations using a finite-element technique. The results from MAXWELL-2D are input to the OOPIC code that tracks the particles throughout the discharge chamber. OOPIC was developed by the Plasma Theory and Simulations Group at the University of California at Berkeley and Tech-X Corporation. OOPIC was not designed for modeling the performance of an ion

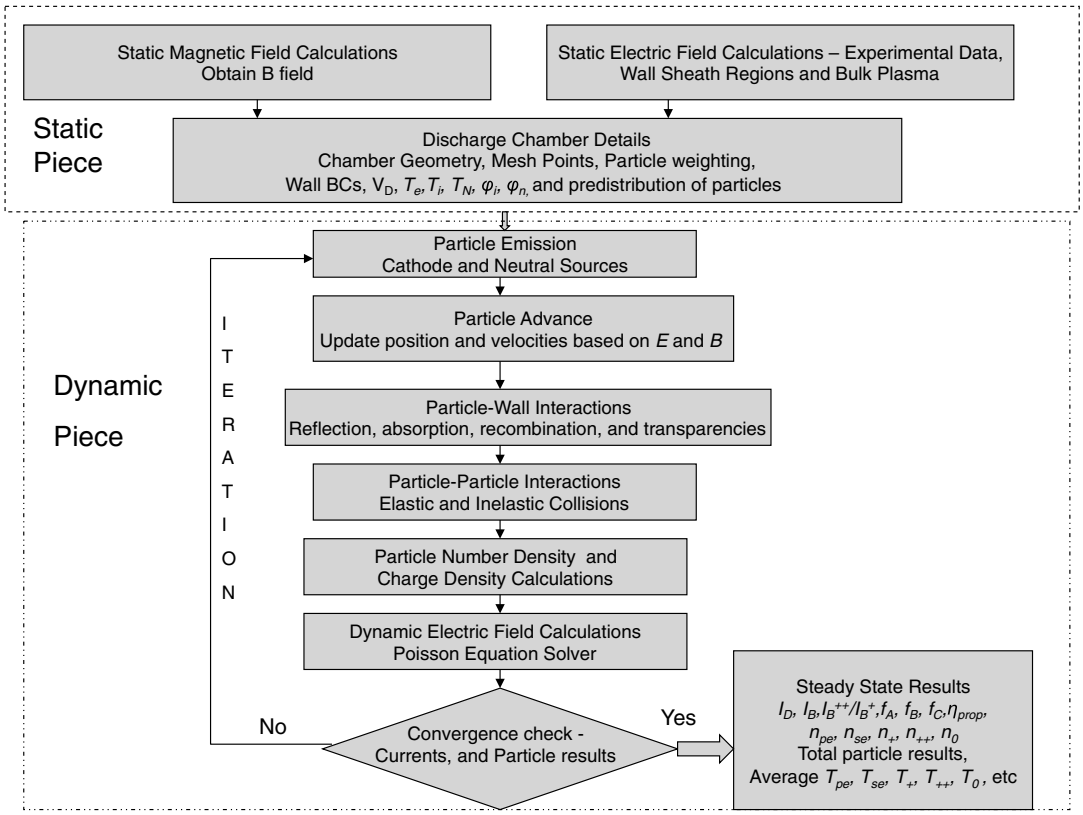

Fig. 3 A flow chart of PIC-MCC model showing the computing sequence of an ion engine discharge chamber plasma simulation.

engine; but it was designed to perform high energy and low density plasma simulations. As part of this work, parts of the code were modified to make them more suitable for ion engine discharge chamber modeling. Also new features were added in OOPIC to handle tracking of neutrals, doubly charged xenon ions, and the coulomb interactions between electrons and ions inside the discharge chamber. Since dynamic neutrals are considered in the OOPIC code, the MCC routines were extensively modified to account for proper calculations of electron-neutral and electron-ion collisions [11]. More details of the modifications can be found in the dissertation work of Mahalingam [23].

Standard PIC-MCC steps [31] are adopted in this work to perform the dynamic piece of the discharge chamber simulation using OOPIC. A two-dimensional finite difference scheme is used for solving the fields and for tracking the plasma particles inside the discharge chamber. The computational mesh can be either a uniform or a nonuniform grid. In this research, both are used. The nonuniform grid is used to perform all calculations in the PIC-MCC simulation. The uniform grid is used for the post processing application of smoothing the results. Figure 4 shows a computational mesh used in this work on the NSTAR discharge chamber. Using the nonuniform grid in the PIC-MCC calculations allows for higher spatial resolution in regions where the fields have large gradients, while saving computer time by using lower resolution in regions where the fields are more uniform. Particles are tracked as macroparticles inside the discharge chamber and each super particle is set to represent billions of real particles. A second order leap frog scheme along with a Boris technique [8] is used for tracking the plasma particles which considers both electric and magnetic field effects. A null collision MCC technique [32] is used for handling the particle-particle interactions inside the discharge chamber. The dynamic electric potentials are solved using a parallel DADI Poisson solver [7]. Parallel processing is enabled in the dynamic piece of the simulation to speed up the computations. More details of the numerical procedures used in this work are given in the dissertation of Mahalingam [23] and in the AIAA paper by Mahalingam and Menart [11].

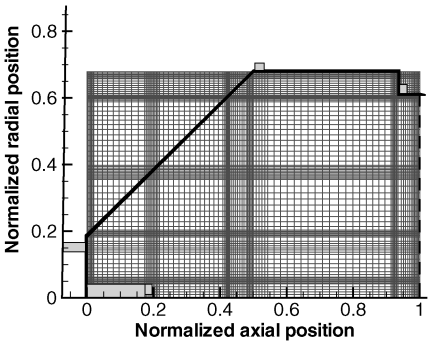

a) Nonuniform computational mesh used in PIC-MCC

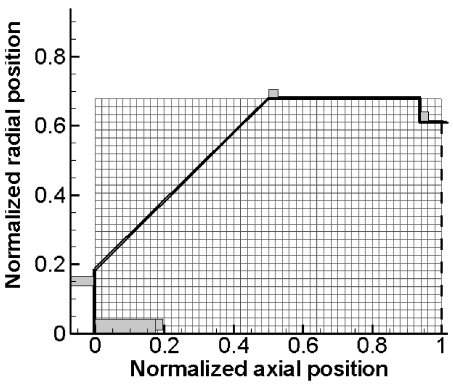

b) Uniform mesh for post-processing

Fig. 4 Computational meshes considered in the PIC-MCC simulation.

The numerical parameters such as grid spacing and time step are selected in this PIC-MCC simulation based on the stability conditions posed by the Debye length and plasma frequency. The explicit particle advancing scheme [8] is limited by the following constraint on the time step size:

$$\omega_{\text{pe}} \Delta t_e \leq 2 \tag{21}$$

where ω_{pe} is given by

$$\omega_{\text{pe}} = \sqrt{\frac{n_e |e|^2}{\varepsilon_0 m_e}} \tag{22}$$

The constraint for grid spacing is given as [8]

$$\frac{\lambda_D}{\tilde{\Delta}} \geq 0.3 \tag{23}$$

where λ_D is the Debye length

$$\lambda_D = \sqrt{\frac{\varepsilon_0 k_B T_e}{n_e |e|^2}} \tag{24}$$

and $\tilde{\Delta}$ is the two-dimensional characteristic grid spacing given by

$$\tilde{\Delta} = \left[\sqrt{\frac{1}{\Delta z^2} + \frac{1}{\Delta r^2}} \right]^{-1} \tag{25}$$

The constraint on grid spacing is required to control plasma heating [8]. Numerical heating causes a nonphysical energy growth in the electrons. Both the plasma frequency and the Debye length are proportional to the particle (electron) number density values and electron temperature values. If a high plasma density is encountered, the simulation needs to deal with a high plasma frequency and a small Debye length. This demands smaller time steps to reduce the plasma oscillations, and a much finer mesh to resolve the Debye length. Both of these factors result in an exponential growth in computational times.

At this point in time, given the speed of computers, it is not practical to perform a discharge chamber sized PIC-MCC simulation of a plasma that has densities over $n_e = 10^{19}$ m^{-3} with electron energies below $T_e = 50$ eV. Using these n_e and T_e values in Eqs. (23) and (24), the computational grid spacing value is found to be on the order of few microns and the computational domain required for resolving the NSTAR discharge chamber is a few hundred million cells (considering 10^3 grid points in each directions). This is a large number of computational cells and is not practical for a detailed PIC-MCC discharge chamber simulation. Thus we set the plasma Debye length to be in the millimeter range instead of micron range (by a factor of 1000) by adjusting the permittivity. To do this the permittivity value needs to be inflated by a factor of 10^6 ($\lambda_D \sim \varepsilon_0^{1/2}$). In this work we keep the artificial permittivity at 1.08×10^{-5} F/m ($\zeta = 1.22 \times 10^6$) which allows the grid size to be increased by a factor of 1100. This scaling allows us to consider a grid spacing value on the order of few tenths of a millimeter instead of few microns and consider a computational domain with 10^4 cells instead of 10^8. This is the difference between obtaining a solution in three months as opposed to three years. The only place where the increased ε_0 affects the simulation is in the Poisson solver for the dynamic fields.

In addition, the grid spacing, $\tilde{\Delta}$, and time step value, Δt, are still restricted by the particle Courant condition:

$$\frac{v_t \Delta t}{\tilde{\Delta}} \sim 0.5 \tag{26}$$

This stability condition ensures that the plasma electrons do not cross more than one cell during a time step. The $\triangle t$ value is also restricted by the MCC accuracy condition. It is given by [33]

$$P \sim (n\sigma(v_t) v_t \triangle t)^2 \ll 1 \tag{27}$$

where P is the probability, n is the target particle number density, and $\sigma(v_t)$ is the total collision cross section. This MCC accuracy condition eliminates missing collisions per time step and the time step size is selected such that few collisions per time step are missed.

The particle grouping is also a factor in maintaining the stability of the PIC-MCC simulations. Numerical noise caused by particle grouping [34] is proportional to $\sqrt{1/N_{\text{cp}}}$. Thus a proper selection of particle weighting has to be made to keep the numerical noise under control. To reduce the statistical noise, more macroparticles should be used, i.e., each macroparticle should represent fewer physical particles. Since more macroparticles means longer computational times, a balance between these two conflicting criteria is made.

IV. NSTAR TH-15 Results

The NSTAR discharge chamber is shown in Fig. 5. Both axial and radial dimensions of the NSTAR discharge chamber are shown in nondimensional units. The discharge chamber length was used for nondimensionalizing the axial and radial directions. The discharge chamber wall material is modeled as aluminum (as in the functional model thruster of a NSTAR discharge chamber [35]) and the permanent magnets on the discharge chamber walls are made of samarium cobalt. The discharge chamber cathode assembly includes both the hollow cathode and the cathode-keeper enclosure. A small primary electron source is placed at the exit of the hollow cathode orifice. The same source is used to model the neutral xenon flow through the cathode. Both primary electron and neutral emission sources have a 30 ° full-angle flow stream directed towards the screen grid. This angular distribution of emission seems reasonable given the chamfered edges of the cathode orifice plate as used in the NSTAR discharge chamber. The main neutral xenon injection site is located in the corner along the side wall and front flange. The neutral propellant from this source also has a 30 ° angular distribution. The molybdenum screen and accelerator grid plates used on the NSTAR discharge chamber are circular disks that have been concaved slightly to reduce thermal buckling problems. In this work only the screen grid is modeled, and it is taken as being flat for simplicity's sake. All three magnets, the cathode source, the main neutral xenon emission location, the discharge chamber walls, and the screen grid are labeled in Fig. 5.

The NSTAR discharge chamber was operated over 16 point throttling levels (TH-0 to TH-15) which vary power levels, neutral flow rates, and thrust conditions. The TH-0 level indicates the low power condition and the TH-15 level indicates the high power condition. In this work the NSTAR TH-15 throttle level is taken as the operating condition for all PIC-MCC simulations. In our earlier work [11], the TH-12 throttle level was used. Table 2 lists the TH-15 operating conditions and performance parameters.

The computational mesh used for the PIC-MCC simulations is given in Fig. 4a.

A. Static Fields

Figure 6a shows the static electric potential mapping used for the TH-15 operating condition. This electric potential mapping uses the experimental measurements of Herman and Gallimore [35]. Herman made these measurements for locations near the cathode keeper to 0.56 nondimensional units upstream of the back wall and radially traversing from thruster centerline to the slant wall. His measurements indicate that the bulk of the discharge chamber plasma potential is at 28 V (for radial locations greater than 0.12 nondimensional units). This is what is used in this work and it is considered for the region axially between 0.2 to 0.5 nondimensional

Table 2 NSTAR TH-15 Operating Conditions and Input Parameters

Description	TH-15
P_{IN}	2.29 kW
T	92.4 mN
I_{sp}	3120 s
η_t	0.618 s
V_D	25.14 V
I_D	13.13 A
$\dot{m}_{\text{main}}$	23.43 sccm
$\dot{m}_{\text{cathode}}$	3.70 sccm
I_E	12.7 A
I_B	1.76 A
V_B	1100 V
V_{Acc}	−180 V
η_{prop}	90%
φ_{ion}	0.84
φ_0	0.13
V_{bulk}	28 V
V_C	2 V
$T_{\text{pe,init}}$	2 eV
T_0	0.0365 eV
t_s	3.2 mm

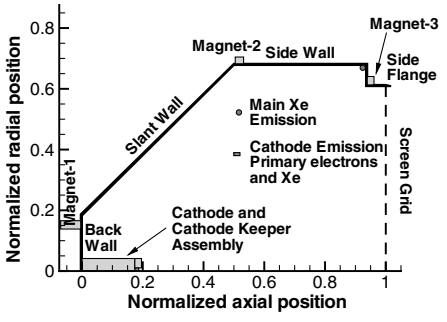

Fig. 5 A schematic of the NSTAR 30-cm diameter discharge chamber.

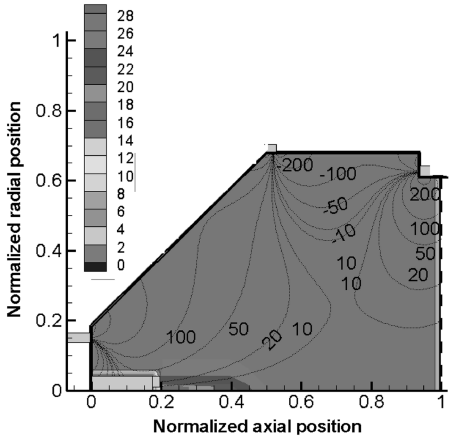

a) Input static electric potential contours in volts

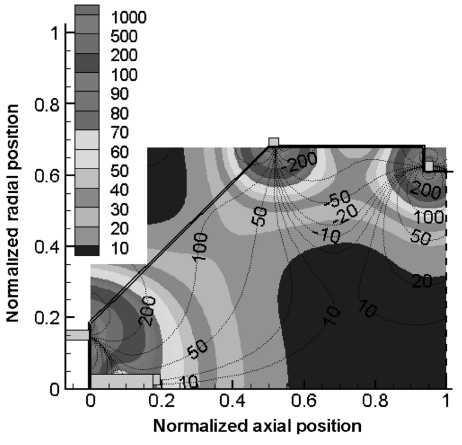

b) Magnetic flux density contours in Gauss. Also shows magnetic vector potential contours (line) in Gauss-cm

Fig. 6 Static fields used for NSTAR TH-15 operating condition.

units from the back wall and radially from the thruster centerline to 0.1 nondimensional units. The electric potential values for the region axially between 0.5 to 0.55 nondimensional units and radially between 0.1 to 0.12 nondimensional units are interpolated to have a smooth transition of electric potential values from the region which uses the experimental data to the bulk plasma. All discharge chamber walls are covered with a sheath that has a thickness of 3.2 mm [23], in which the 28 V bulk plasma potential drops to the 25.14 V wall potential. Since the bulk plasma potential is maintained at 28 V and the cathode source is maintained at 2 V, there is a 26 V rise from the cathode to the bulk plasma. The initial primary electron kinetic energy [36] from the cathode tip is set to 2 eV and the neutral particle kinetic energy is set to 0.0365 eV. The sum of the 2 eV primary electron's initial kinetic energy and the 26 eV potential energy provides an energy input for the primary electrons of 28 eV, the bulk plasma potential value. The cathode keeper is maintained at 6 V positive to the cathode and the screen grid is maintained at 0 V.

Figure 6b shows the static magnetic field inside the NSTAR discharge chamber. In the axial direction the magnetic flux density values are low for a region from 0.25 nondimensional units downstream of the cathode keeper to the screen grid. In the radial direction the magnetic flux density values are low from the thruster centerline to a radius of 0.45 nondimensional units. This can be looked at as a field free region. In Fig. 6b the magnetic vector potential contour lines (magnetic field lines) are superimposed on the flux density contour plot. The magnetic vector potential lines run between the cusp regions of the magnets. The slanted wall of the discharge chamber is covered by the 100 G-cm magnetic vector potential line running between magnet-1 and magnet-2. This 100 G-cm line leans towards the slanted wall at an axial position between 0.3 to 0.42 nondimensional units and a radial position between 0.25 to 0.5 nondimensional units. This wall region is mentioned because this is a weak spot in the confining magnetic field and it is believed that this effects the NSTAR performance.

B. Results Convergence

A convergence study is conducted with the developed PIC-MCC simulation for all numerical parameters in the simulation. The convergence is checked in terms of the current results and the particle number density distribution results. The converged numerical parameters are

$$W_{\text{macro}} = 1.25 \times 10^{11} \text{physical particles}, \qquad N_{e,\text{cell}} = 35$$

$$\Delta t_e = 5 \times 10^{-10}\ \text{s}, \qquad \Delta t_{\text{ion}} = 5 \times 10^{-8}\ \text{s}, \qquad \Delta t_{\text{Xe}} = 1 \times 10^{-7}\ \text{s}$$

$$N_z = 100, \qquad N_r = 82, \qquad N_{\text{cell}} = 8200$$

$$N_{\text{iter,ch arg}\,e} = 10\text{–}20 \times 10^6, \qquad N_{\text{iter,Xe}} = \sim 100 \times 10^6$$

Details of the numerical parameter convergence study are given in the dissertation work of Mahalingam [23].

Figure 7a shows the total number of Xe, Xe^+, Xe^{++}, primary electrons, and secondary electrons in the discharge chamber as a function of the number of iterations used by the PIC-MCC simulation. A previous PIC-MCC solution is used as an initial guess of the particle distributions for this case. From Fig. 7a it can be seen that the simulation has achieved a steady state condition in which the solution converged within 5%. All the charge particles plotted in Fig. 7a show this. The total number of iterations for which the particles are tracked is about 100 million. Figure 7b shows the beam current and discharge current results for the discharge chamber as a function of the number of iterations. Both current results indicate that the simulation has reached steady state. The initial condition in this simulation is taken from a previous PIC-MCC simulation's solution which is observed to be closer to the end results. That is the reason why the charge particles and currents are relatively flat in Figs. 7a and 7b. Figure 8 shows the effect of starting the computation at different locations. The convergence plots in Figs. 7a and 7b used a starting point like that shown for starting point (SP) 2 curves in Fig. 8. Figure 8 clearly shows that the convergence of the results is independent of the starting point.

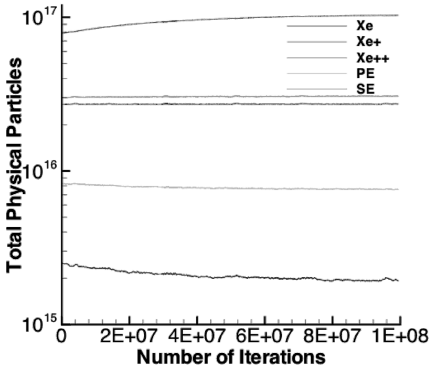

a) Total physical particles

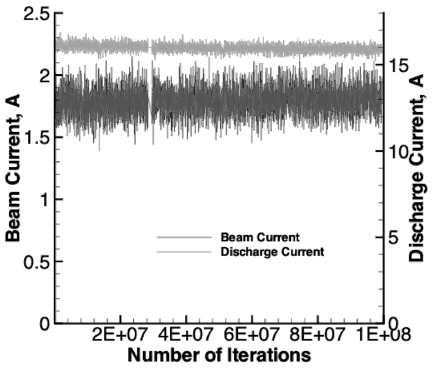

b) Beam current and discharge current

Fig. 7 Iteration convergence of NSTAR discharge chamber operating under TH-15 throttle level.

The results in Fig. 7a indicate that all charge particles require about 5 million iterations to reach a steady state condition. The high energy primary electrons are the first to reach convergence. The heavier ion particles and the secondary electrons take a long time to reach convergence compared with the primary electrons. The ions and secondary electrons are produced inside the discharge chamber from the ionization collisions of high energy electrons. At every ionization location both species are produced. The results of the secondary electrons and ions are somewhat coupled because the bulk of the secondary electrons in the discharge chamber come from ionization events. The dynamic electric fields also couple the two particle types together. The secondary electrons move faster because of their lower mass and try to move away from the ions. However, the dynamic electric field effect pulls the secondary electrons to the ion locations to balance the charge difference.

The neutral particles shown in Fig. 7a take many iterations to reach convergence as compared with the number of iterations required for

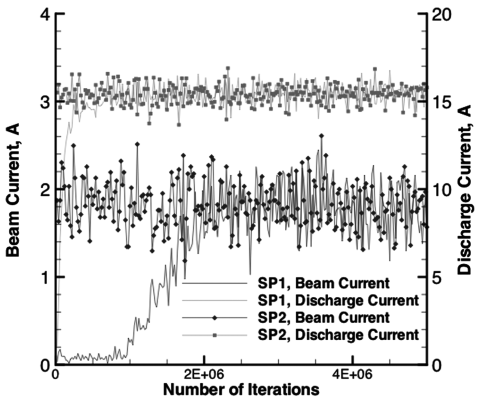

Fig. 8 Comparisons of beam and discharge current results vs number of iterations for the two different SP cases.

the charged particles to reach a converged state. A couple of reasons for this are that the neutrals move slower than the ions and ions tend to be created at many different positions throughout the discharge chamber. On the other hand, the bulk of the neutrals have to travel from their source points (emission locations) to the location where a steady state distribution is maintained in the bulk of the discharge chamber. The small changes seen in the neutrals as a function of time are difficult to eliminate. To get the neutral particles to full convergence about 100 million iterations, i.e., 50 milliseconds, is required. The wall-clock time taken for the simulation to perform 100 million iterations is nearly 2.5 months on ten CPUs.

C. Experimental Validation

In this section the numerical results are compared with experimentally measured data. The experimental data for the NSTAR TH-15 condition are obtained from a number of sources [37–43].

Current comparisons are given in Table 3. The beam current and the propellant utilization efficiency results are found to be in very good agreement with the experimental data. The beam current [38,44] and the propellant efficiency compare within 2%; but the I_B^{++}/I_B^{+} ratio differs from the maximum experimental results [40] by 30%. The maximum double-to-single ion ratio of 0.34 was measured by Polk et al. [40] on the high power throttle tests performed during the NSTAR 8000 h ion engine endurance test. In other experimental studies [41] the ratio of double-to-single ion current in the beam was reported in the range 0.15 to 0.27. The double ion comparison indicates that the present plasma model is slightly over predicting the number of double ions in the beam current. The doubles-to-singles ratio are actually measured at different locations in experiments (the $E \times B$ probe is placed 6 m from thruster exit) and in the numerical simulations (computed right at the screen grid exit). This is a major difference between experimental and numerical results for the doubles-to-singles ratio. The charge-exchange and recombination collisions that occur in the plume region can affect the double ion population measured at 6 m from the thruster exit. This work only includes the discharge chamber region in the simulation. Hence it is not possible to investigate the effects of charge-exchange and recombination processes in the plume region. The calculated discharge current differs from the measured value by 22%.

The discharge current value is based on the difference between the rate of electrons collected at the anode-biased walls and the rate of ions collected at the anode-biased walls. From the plasma model the total ion current collected at the chamber walls is 0.78 A. The experimentally estimated ion currents to the anode and screen grid on an NSTAR-type ion thruster [43] is 2.5 A. An estimate of the anode-biased wall ion current can be obtained by subtracting an average experimentally determined screen grid ion current (0.40 A) from the 2.5 A anode and grid current. This gives an anode-biased wall ion current of 2.1 A. This is significantly higher than the 0.78 A predicted by this model. It is believed the reason for this difference is the electrical potential distribution used. The electric potential field used in this work does not produce any significant gradients except in small regions close to the walls mimicking sheaths and in the cathode region. Important potential gradients controlling ion flow to the walls would be a presheath region. A presheath region would accelerate ions out of the plasma into the anode-biased walls. When ions hit the anode-biased walls the discharge current is reduced. A presheath region would also hinder the flow of electrons to the anode-biased walls. This also would lower the discharge current. Future work should look into applying a presheath potential in regions close to anode-biased walls.

The effectiveness of ions produced inside the discharge chamber is measured in terms of plasma ion production cost, ϵ_p, and the beam ion production cost, ϵ_B. The plasma ion production cost is given by

$$\epsilon_p = \frac{I_D V_D}{I_P} \tag{28}$$

where I_P is the total ion production rate inside the discharge chamber. The total ion production current in the discharge chamber is based on the total ion currents collected at the various chamber walls and the ion currents to the beam. The ion production current as given by Brophy and Wilbur [45] and Foster et al. [43] is

$$I_P = I_A + I_B + I_C + I_{\mathrm{SG}} \tag{29}$$

This computed total ion production current is found to be 5.74 A. The beam ion production cost is computed using

$$\epsilon_B = \frac{V_D I_D}{I_B} \tag{30}$$

The computed plasma ion production cost and beam ion production cost, as well as other global performance parameters, are compared with experimental values [40,41,43] in Table 4. The plasma ion production cost compares within 7% and the beam ion production cost compares within 16% of the average experimental values.

The ideal thrust produced by the ion engine discharge chamber depends on the beam current and beam supply voltage. It is given as

$$T_{\mathrm{ideal}} = \sqrt{2\frac{m_{\mathrm{ion}}}{|e|}} I_B \sqrt{V_B} \tag{31}$$

The computed beam current is 1.78 A and from the NSTAR throttle table (see Table 4) the beam supply voltage, V_B, for the TH-15 throttle condition is found to be 1100 V. This quantity is not predicted by the plasma model because the region where this is applied is outside the discharge chamber computational domain. Substituting these values into Eq. (31) gives an ideal thrust value of 97.5 mN. However, the actual thrust produced in the ion engine discharge chamber is affected by the presence of double ions in the beam and the beam divergence factor. It is given by

$$T_{\mathrm{actual}} = \alpha F_t T_{\mathrm{ideal}} \tag{32}$$

Here the double ion correction factor, α, is based on the ratio of double-to-single ion current in the beam current which is given by

$$\alpha = \frac{(1 + \frac{1}{\sqrt{2}}\frac{I_B^{++}}{I_B^{+}})}{(1 + \frac{I_B^{++}}{I_B^{+}})} \tag{33}$$

The computed α value is found to be 0.91. Substituting this α result, the beam divergence factor of $F_t = 0.98$ obtained from experiments [46], and the ideal thrust result into Eq. (32) gives a thrust value of 87 mN. The experimentally calculated thrust result was 92.4 mN and our thrust value differs by 5% from the experimental result. This difference is mainly influenced by the higher double ion ratio predicted in simulations.

The specific impulse of the ion engine discharge chamber is computed based on the actual thrust value and the total propellant mass flow rate value. It is given by

Table 3 Comparisons of numerical discharge chamber current results with experimental measurements for the TH-15 operating condition

Discharge Parameters	I_B	I_B^{++}/I_B^{+}	η_{prop}	I_{SG}	I_D
Units	A	——	%	A	A
Numerical results	1.78	0.44	91.4	0.33	16.0
Experimental data	1.76	0.15–0.34	90	0.37–0.43	13.1

Table 4 Comparisons of numerical results with experimental measurements for the discharge chamber performance parameters of TH-15 operating condition

Discharge parameters	ϵ_p	ϵ_B	T_{actual}	I_{sp}	η_t
Units	W/A	W/A	mN	s	%
Numerical results	70	226	87.0	2930	0.55
Experimental results	76	190–200	92.4	3120	0.618

Table 5 Total particle results at steady state for the NSTAR discharge chamber at TH-15 operating condition

Steady-state results	Xe	Xe^+	Xe^{++}	Primary	Secondary
N_{phys}	10.3×10^{16}	3.06×10^{16}	0.196×10^{16}	0.76×10^{16}	2.72×10^{16}
$\bar{n}$, m^{-3}	8.25×10^{18}	2.46×10^{18}	0.16×10^{18}	0.61×10^{18}	2.18×10^{18}
T_{avg}, eV	0.0324	0.047	0.104	3.90	2.45

$$I_{sp} = \frac{T_{actual}}{\dot{m}_p g} \tag{34}$$

The total propellant mass flow rate for the discharge chamber is based on the sum of the neutral flow rate through the cathode, the main plenum, and the neutralizer cathode. The total flow rate for the NSTAR TH-15 throttle condition is found to be 3.02×10^{-6} kg/s. Substituting the computed actual thrust of 87 mN and the total mass flow rate of 3.02×10^{-6} kg/s into Eq. (34) gives a specific impulse of 2930 s. Once the values of T_{actual} and I_{sp} are known, the overall thruster efficiency, η_t is computed as

$$\eta_t = \frac{T_{actual} I_{sp} g}{2P_{IN}} \tag{35}$$

The input power value for the calculation of η_t is taken from the NSTAR throttle table (see Table 4). The overall thruster efficiency is computed to be 55% which differs from experimental result by 11%.

Next a comparison between the beam profile results obtained from the numerical simulation and from experiments is made. The numerical beam current density results are presented in two forms following the technique used by Wirz [47]. In the first form, the beam current density called $jB++$ is computed by summing the ion current due to singly charged ions (Xe^+) and doubly charged ions (Xe^{++}). In the second form, the beam ion current is called $jB+$, and is computed by summing the value of the single ion current and half the value of the double ion current. The first form looks at the beam current as the number of unit charges leaving the grid. This is the physically correct way to look at the beam current. The second form looks at the beam current as the number of positively charged particles leaving the grid. The second form is useful for studying the relative contribution of double ion current to the total beam current.

Figure 9 shows the beam current density values obtained from the numerical simulation and from measured data taken during an NSTAR wear test [41]. The computed beam current density results are obtained right at the screen grid location, while the experimental data is obtained downstream of the accelerator grid [41]. The profile which should be compared with the experimental results is $jB++$. Note that the $jB+$ profile compares better to the experimental results. This exemplifies our observation that the numerical simulation is producing too many double ions. The computed beam current density profiles are highly peaked near the centerline compared with the experimental results. The experimental values may have been more peaked at the centerline if they were taken at the same location at which the numerical results were taken. Measuring the beam current density downstream of the accelerator grid may reduce the peak. In addition, charge-exchange collision processes between ions and neutrals may lower the number of ions reaching the downstream location where the experimental data is measured. Another difference between the calculated and experimental beam current profiles was that the experimental results were obtained using a screen grid that has a slight curvature. This curvature is not included in the grid boundary condition used in the modeling work. The oscillations seen in the calculated results are due to statistical variations present in the PIC-MCC simulation. These are reducible by using more computational particles.

In our numerical simulation, the F_B value for the $jB++$ beam current density profile is found to be 0.39 and the F_B value for the $jB+$ beam current density profile is found to be 0.44. The experimentally reported F_B value is 0.46 [41].

D. Plasma Particle Results

Table 5 shows the steady state results for the total number of each type of particle, N_{phys}, present inside the discharge chamber for each species. These results indicate that the ionization fraction of the plasma is 26% and the ratio of the total number of double ions (Xe^{++}) to single ions (Xe^+) is 0.064. This is much lower than the double-to-single ion current ratio, 0.44, obtained at the grid. The total number of primary electrons is 23% of the total number of electrons. These total particle results also indicate that the total number of negative charges (sum of primary and secondary electrons) are nearly equal to the total number of positive charges (sum of Xe^+ and twice Xe^{++}). The ratio of the negative charges to the positive charges is 1.01. This corresponds to a net negative coulomb charge of -5.4×10^{-5} C or 3.4×10^{14} electrons. This is less than 1% of the total electron particles in the discharge chamber. This is a strong indication that the dynamic electric field solver with an inflated plasma permittivity is performing the function it was intended to do, maintain an overall plasma charge of zero.

Table 5 also shows the steady state volume averaged particle number densities and kinetic energy results for each species. As expected the primary electrons have the highest energy, the secondary electrons the next highest, then Xe^{++}, Xe^+, and Xe.

Next, the steady state plasma particle number density results for the TH-15 operating condition are given. Also the steady state kinetic energy distribution results are given for the primary electrons. All particle distribution plots have the magnetic vector potential lines (in gauss-cm) superimposed on them so the reader can judge the effects of the magnet field on the particles. Comparisons of the particle number density results are made with the experimental results obtained by Herman [48] and Sengupta et al. [49,50] on the NSTAR thruster.

Figure 10a shows the steady state neutral gas number density results. The maximum neutral number density value is observed near the cathode-keeper exit, ($\sim 1 \times 10^{20}$ m^{-3}), where the cathode neutral particle source is located. This number density result is higher than the neutral number density result observed at the main plenum source for neutrals ($\sim 2.0 \times 10^{19}$ m^{-3}). One reason for this higher number density is the small emission volume at the cathode as compared with the main plenum emission. In an axisymmetric, cylindrical coordinate system the volume at a given radial location is proportional to r. The cathode emission is focused while the main plenum emission is more diffuse. Another reason for getting a peak number density value at the cathode exit is because of ion

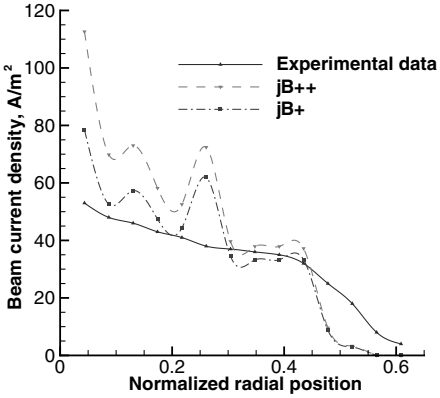

Fig. 9 Beam profile for the NSTAR TH-15 operating condition. Comparison between the numerical results and the experimental data are also shown in this plot.

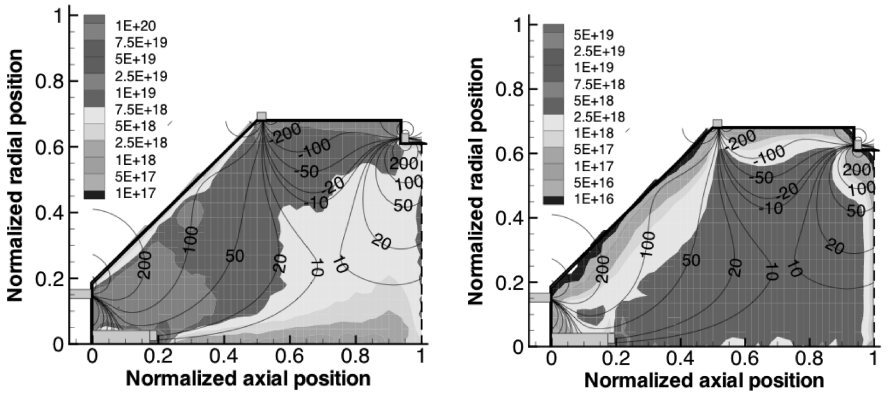

a) Xe number density in m^{-3}

b) Xe^{+} number density in m^{-3}

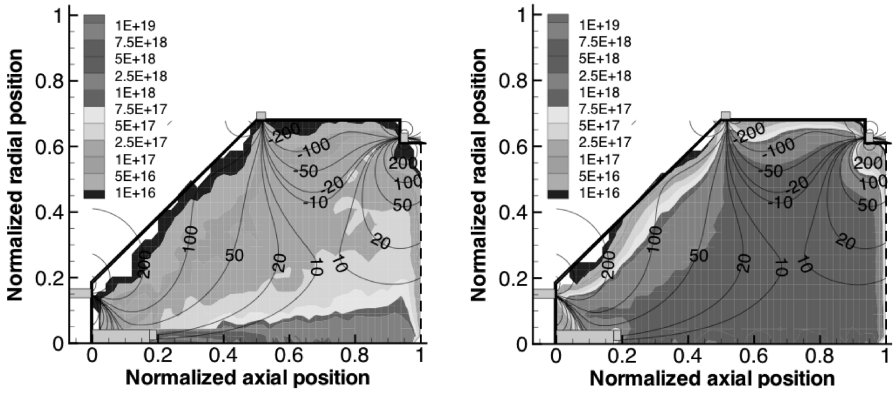

c) Xe^{++} number density in m^{-3}

d) Secondary electron number density in m^{-3}

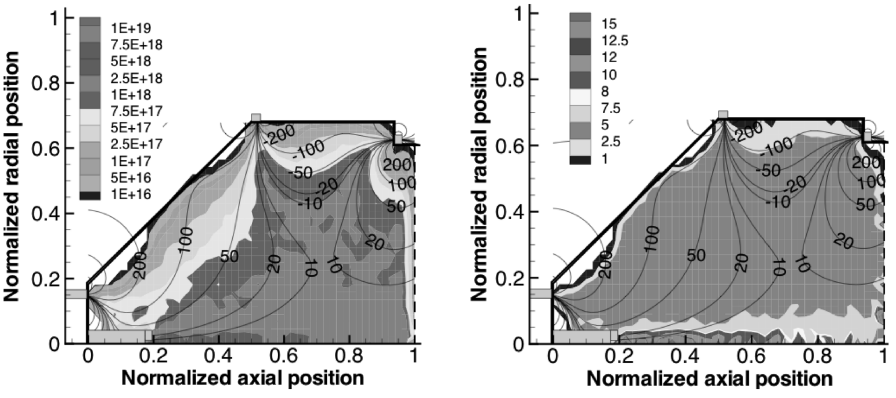

e) Primary electron number density in m^{-3}

f) Primary electron energy in eV

Fig. 10 Particle distribution results at steady state for NSTAR TH-15 operating condition. The magnetic vector potential lines (in gauss-cm) are superimposed on these plots to judge the effects of the magnet field on the particles.

recombination at the cathode wall surfaces. Ions made in the plasma close to the cathode emission source have a propensity to travel back towards the cathode, because of its lower electrical potential. This increases the number of neutral particles present in this region. The side wall region has a neutral number density of 1×10^{19} m^{-3}, because there are few high energy electrons in this region and also due to wall recombination of ions. The high side wall neutral number densities are also the result of the neutrals coming from the main plenum source. The most interesting aspect of the neutral number density distribution results is the depletion of neutrals along the centerline of the discharge chamber. Most of the plasma along the centerline is more than 90% ionized. This neutral particle depletion is reported in a relative neutral number density study done by Sengupta et al. [50]. This depletion occurs because of the high energy primary electrons coming from the cathode. The magnetic field enhances this problem by keeping electrons confined to the centerline region. If these electrons could be forced off the centerline quicker, a better performing ion engine would be the result.

Figure 10b shows the steady state Xe^{+} number density results. At the cathode source a maximum Xe^{+} number density value of $\sim 5 \times 10^{19}$ m^{-3} is observed. At the exit of the cathode keeper the number density value is observed to be 1×10^{19} m^{-3} which is in agreement with plasma number density results given by Herman [48]. The experimental measurements by Herman show a sharp decrease in the number density values in the conical section while our Xe^{+} number density results show no decrease in number density values in the radial direction until after 0.16 nondimensional units. Our number density results are in agreement with the electron number density results given by Sengupta et al. [49] who had made a similar measurement in the conical section of an NSTAR-type thruster. The number density values decrease rapidly, by 2 orders of magnitude, in the region between axial positions of 0.2–0.5 nondimensional units and radially in the conical section after 0.16 nondimensional units. The minimum Xe^{+} number density value in the slanted wall region is observed to be 1×10^{16} m^{-3}. This result is in agreement with experimental studies [43,48–50]. In the cylindrical section, the Xe^{+}

number density values are found to be in the range between 2.5×10^{18} m^{-3} and 5×10^{18} m^{-3}. The Xe^{+} number density values in the cylindrical section decreases after 0.58 nondimensional radial units and show an order of magnitude decrease in the number density values near the side wall region. The minimum Xe^{+} number density value in the side wall region is observed to be 2.5×10^{17} m^{-3}. At the screen grid, the ion number density values are observed to be smaller. This is mainly because the ions are accelerated to a high speed by the presence of large electric fields in the screen grid sheath. The white regions inside the discharge chamber boundaries are regions where no computational particles exist. This does not mean there are no real particles present here; however, it does mean that the number of real particles present is extremely small.

Figure 10c shows the steady state Xe^{++} number density results. Xe^{++} has its highest number densities ($\sim 1.25 \times 10^{19}$ m^{-3}) between the cathode keeper and 0.15 nondimensional units axially downstream of the cathode keeper. These number densities may increase the erosion of the cathode and cathode-keeper walls as discussed in experimental studies [51,52]. The Xe^{++} number density values decrease sharply in the radial direction. In the conical section the Xe^{++} number densities decrease rapidly in the radial direction which indicates fewer double ionization events compared with the cylindrical section. In the cylindrical section axially between 0.5 to 0.9 nondimensional units and radially from the thruster centerline to 0.12 nondimensional units, the Xe^{++} number density values are found to be in the range between 1×10^{18} and 2.5×10^{18} m^{-3} which is about 0.3–0.8 times the Xe^{+} number density values in these locations. These high Xe^{++} number density values radially near the thruster centerline and axially a few centimeters upstream of the screen grid indicate that the beam current density along the thruster centerline is peaked by the Xe^{++} ions. The formation of such a large Xe^{++} number density along the thruster centerline is due to high energy primary electrons concentrated along the thruster centerline.

Figure 10d shows the steady state secondary electron number density results. High secondary electron number density values of 5×10^{18} m^{-3} are found for the axial positions between 0.3 to 0.8 nondimensional units and close to the thruster centerline in the radial direction. The secondary electron distribution results in Fig. 10d indicate that the secondary electrons are confined by the magnetic field lines. In the conical section, the number density values drop radially after 0.2 nondimensional units. The minimum secondary electron number density value near the slanted wall is found to be in the range of 5×10^{16} m^{-3}. In the cylindrical section for the regions axially between 0.5 to 0.9 nondimensional units and radially between 0.05 to 0.58 nondimensional units, the secondary electron number density values are found to be in the range of 3×10^{18} m^{-3} -4×10^{18} m^{-3}. The secondary electron number density values decrease for regions radially after 0.58 nondimensional units because of confinement by the strong magnetic field lines. At the side wall the secondary electron number density values are found to be in the range of 1×10^{17} m^{-3} -3×10^{17} m^{-3}. These results qualitatively agree with the experimental measurements made by Sengupta et al. [50]. In the bulk of the discharge chamber the calculated secondary electron number density results are higher than the experimental values.

Figure 10e shows the steady state primary electron number density results. Maximum primary electron number densities are observed near the cathode-keeper exit, $\sim 7.5 \times 10^{18}$ m^{-3}. The primary electron distribution results in Fig. 10e indicate that the primary electrons are mostly confined by the magnetic field lines. In the conical section the primary electron number density values decrease rapidly due to the confinement of electrons with the higher magnetic field lines (above 50 gauss-cm) running between the cusps of magnet-1 and magnet-2. One problem in the magnetic field is in the middle of the slanted wall. The 100 G-cm magnetic vector potential line leans into the wall. Primary electron number densities also bow into the wall close to this point. As will be shown latter, this leads to an increased flux of primary electrons to the slanted wall. This region in the magnetic field is called a hole by Bennett et al. [53].

Figure 10f shows the steady state primary electron average kinetic energy results. The maximum local average primary electron kinetic energy values of 12.5–15 eV are found axially between the cathode-keeper exit and 0.15 nondimensional units downstream of the cathode keeper. The radial extent of these energies is from the thruster centerline out to 0.05 nondimensional units. The high energy primary electrons in this region are responsible for the higher Xe^{++} number densities (see Fig. 10c) and the depleted neutral particle number densities in Fig. 10a. The kinetic energy values sharply drop in the radial direction to 5 eV at 0.08 nondimensional units. The bulk of the primary electron average kinetic energies are found to be between 3.5–4 eV. Both conical and cylindrical sections exhibit similar primary electron energy variations. Near the chamber walls the average kinetic energy value is found to be on the order of 1–2.5 eV.

Figure 11 shows the electron energy distribution function (EEDF) for primary and secondary electrons at the steady state condition. This distribution is for all the electrons in the discharge chamber. The electrons are grouped into 0.2 eV energy bins from 0 eV to 30 eV. After counting the number of particles in each 0.2 eV increment, the relative fraction of the particles in each bin is computed by dividing the total number of particles in that energy bin with the total number of particles. Both EEDF results are found to be skewed towards the low electron energy values. The peak of each EEDF is around 1.2 eV. From these peak points the EEDFs drop gradually. The slope is found to be steeper for the secondary electrons than the primaries. The most notable difference between the two plots is the high energy tail of the primary electron EEDF. There is a small fraction of high energy primaries present. Although the numbers of these high energy primaries is small, their importance to sustaining the discharge is high. Only 3.5% of the primary electrons are found to have an energy value of 12.5 eV and above. The ionization threshold energy required for the creation of Xe^{+} from Xe is 12.1 eV. These 3.5% of primary electrons are responsible for the creation of ions inside the discharge chamber. Only 0.8% of the total primary electrons are found to possess more than 21.2 eV of energy, which is the ionization threshold energy for the creation of Xe^{++} from Xe^{+}. About 8.3% of the total primary electrons are found to have electron energies above 8.35 eV and above, which is the excitation threshold for Xe. In the secondary electron group only 0.27% of the electrons are found to have an energy value of 12.5 eV and above. About 1.4% of the secondary electron particles are found to have energies of 8.35 eV and above. As can be seen in Fig. 11 an insignificant number of secondary electrons are found to possess electron energies greater than 21.2 eV. The EEDF functions displayed in Fig. 11 point out that a relatively few number of electrons are sustaining the plasma inside the discharge chamber.

E. Particle Loss Mechanisms

It is interesting to know how different inelastic collision processes affect the high energy primary electrons, and the slow moving secondary electrons inside the discharge chamber. Table 6 lists the relative percentages of each of the inelastic collision processes

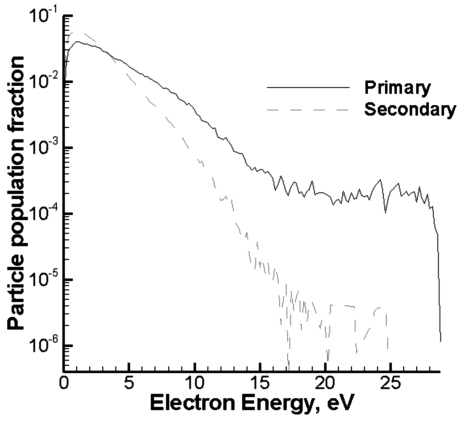

Fig. 11 Electron energy distribution function for both primary and secondary electrons at steady state for the NSTAR discharge chamber.

included in this PIC-MCC simulation. The results are for both primary and secondary electrons at the steady state condition.

These results show that the most common collisions are those with neutral particles. This is understandable because the neutrals are the most plentiful species in the discharge chamber. As will be shown in the physical parameter study, excitation collisions are a significant means by which electrons lose energy. It would seem that wall losses are also a place where electrons loose a significant amount of energy. The total percentage of electron recombination collisions with Xe^{+} and Xe^{++} is 6.23 %.

To gain a better understanding of the particle losses to the walls of the discharge chamber, current density, j, profiles along each of the walls is plotted. This is done for each charged particle species in Fig. 12. These plots localize the wall areas where particles are being lost. A discharge chamber wall surface can be looked as a combination of the following two segments: 1) a magnetic cusp area (if the wall has a magnet on it) and 2) a noncusp area composed of wall locations between the cusps of two magnet rings. If two adjacent magnets are spaced too far apart then a hole can develop in the magnet field on the surface of the wall. As discussed by Bennett et al. [53], a wall hole is identified as the wall region where the strength of the magnetic field lines becomes weak enough to allow a significant number of electrons to reach the walls. Holes in the magnetic field result in poor ion engine performance [53,54]. The magnetic field strength and magnetic vector potential results for the three magnetic-ring NSTAR ion engine (see Fig. 6) indicate two such hole regions on the discharge chamber wall surfaces. One hole region is found on the slanted wall surface of the conical section (axially between 0.26–0.32 nondimensional units) and the other hole region is found on the side wall of the cylindrical section (axially between 0.68–0.76 nondimensional units). The magnetic field strength values in the hole regions are found to be much weaker than the no-hole regions (15–20 G on the slant wall hole region and 25–30 G on the side wall hole region).

In Fig. 12 the steady state species current densities on the four walls of the discharge chamber (back, slanted, side, and flange) are plotted on three graphs. The slanted wall in the conical section and the side wall in the cylindrical section are combined together and plotted versus the axial location. To minimize the statistical fluctuations in the nonuniform grid results, the plotted wall current densities are taken off the overlaid uniform grid. Current density results are plotted for Xe^{+}, Xe^{++}, secondary electrons, and primary electrons. The discharge chamber wall locations (both axial and radial positions) are given in nondimensional units and the current density results are given in A/m^2. Figure 12a shows the species current density collected at the radial locations of the back wall surface. A maximum current density value is observed for the secondary electrons at the magnetic cusp location (at $r = 0.15$ nondimensional units) on the back wall surface. Similarly the primary electron current density value is found to be larger at the cusp location. Both electron current density values are found to be dropping sharply before and after the cusp region. The secondary electron current density values at the noncusp regions are found to be much smaller and the primary electron current values in the noncusp regions are found to be zero. This occurs because of the strong magnetic field lines at the back wall surface. As shown in Fig. 12a the Xe^{+} ion current density value is found to be 500 times smaller than the secondary electron current density value. The Xe^{++} and Xe^{+} current density results show that both ions are lost at all locations of the back wall surface. The Xe^{++} current density value is found to be smaller than Xe^{+} for most of the radial locations along the back wall. The peak current density values of all species are listed in Table 7.

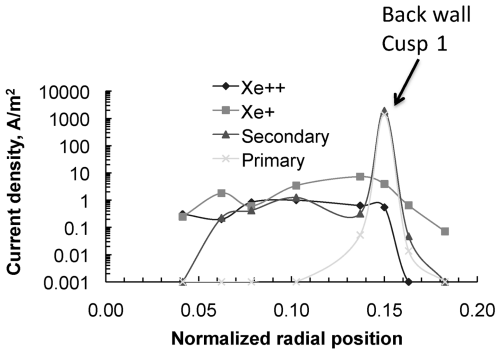

a) Back wall radial surface

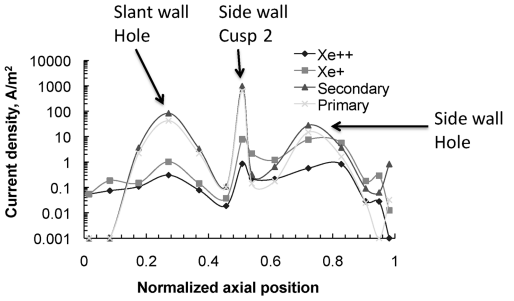

b) Axial wall surfaces (both conical and cylindrical section)

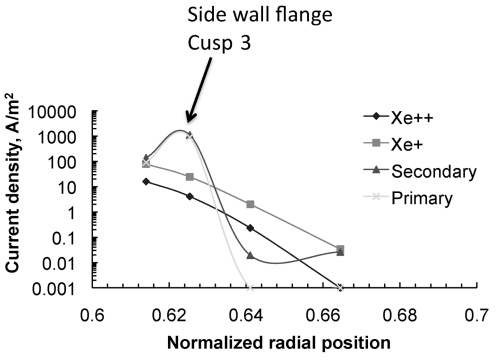

c) Side flange radial surface

Fig. 12 Current density profiles along the walls of the discharge chamber for each of the four different charge particles at steady state for the NSTAR TH-15 operating condition.

Figure 12b shows the species current density results collected at the axial locations of the slanted wall and the side wall of the discharge chamber. The species current density results on the axial wall surfaces are smaller compared with the other radial wall surfaces (see Figs. 12a and 12c). All species current density results are found to peak at three locations as identified in Fig. 12b. The first peak is at the hole region of the slanted wall surface (at $z = 0.27$ nondimensional units), the second peak is at the cusp region of magnet-2 (at $z = 0.51$ nondimensional units), and the third peak is at the hole region of the side wall (at $z = 0.72$ nondimensional units). Out of these three peaks, all species are found to have the maximum current density values at the cusp location. The secondary electron is found to have the largest current density value in all of these three peaks. The maximum current density values for each species in the slanted wall hole region, side wall cusp region, and the side wall hole

Table 6 Percentage of inelastic collision processes for electrons at steady state

Inelastic collision processes	Xe Exc.	Xe Ionz.	Xe^{+} Exc.	Xe^{+} Ionz.	Xe^{+} Recomb.	Xe^{++} Exc.	Xe^{++} Recomb.	Wall Losses
Primary electrons	29.8	15.8	0.66	2.16	0.8	0.22	0.1	16.0
Secondary electrons	4.54	0.75	0.06	0.012	4.76	0	0.58	23.8

Table 7 Maximum species current density values in A/m^2 at various discharge chamber wall surfaces at steady state for the NSTAR TH-15 operating condition

Location details	Xe^{++}	Xe^{+}	Secondary electron	Primary electron
Back wall (Cusp 1)	0.9	7.3	1905.42	1368.67
Slant wall (Hole)	0.305	1.028	83.14	42.25
Side wall (Cusp 2)	0.852	7.85	975.63	624.1
Side wall (Hole)	0.57	7.62	27.9	14.84
Side wall flange (Cusp 3)	16.0	78.37	1103.67	902.67

region are listed in Table 7. The observation of peak current density results in the slanted wall hole region and the side wall hole region further support the findings of the magnetic field strength study conducted by Bennett et al. [53]. Only ion currents are found on the slanted wall surface axially from the discharge chamber to 0.1 nondimensional units. This indicates the magnetic field is sufficiently strong over this portion of the wall to stop electrons from reaching the slanted wall surface. At the slanted wall hole region the current density values of both positive and negative charged particles are found to be high. This indicates a hole in the magnet field. The species current density results axially between 0.37 to 0.5 nondimensional units are found to sharply drop from the slanted wall hole region current density results. The slanted wall's total electron current density is found to be 200% higher than the side wall hole region's total electron current density. The slanted wall hole is more critical to discharge chamber performance than the side wall hole. Design changes can be made to plug these holes in the magnetic field. All species current density results at the side wall region closer to the screen grid (axially between 0.86 to 1 nondimensional unit) indicate that this portion of the side wall is well covered by the magnetic field lines from magnet-3.

Figure 12c shows the species current density results collected at the radial locations of the sidewall flange where magnet-3 is placed. The electron current density results are found to be large at the magnet-3 cusp location (at $r = 0.625$ nondimensional units). Only secondary electron currents are observed radially after the cusp location on the side wall flange. Both Xe^{+} and Xe^{++} ion current density results are found to be large for the regions radially between $r = 0.61$ nondimensional units and $r = 0.625$ nondimensional units. These ion current density results are found to be much higher than the ion current density results observed in the magnet cusp locations on the back wall and the side wall of the discharge chamber. This large increase in ion current density could be due to the proximity of the side wall flange to the screen grid. The maximum species current density values collected at the side wall flange are listed in Table 7.

V. Conclusions

A particle-based plasma model has been developed to model the ion engine discharge chamber plasma in detail. The full kinetic approach used in this work eliminates the typical assumptions considered in fluid based discharge chamber models related to the plasma distributions and particle transport coefficients. Neutrals, first ions, second ions, secondary electrons, and primary electrons are tracked in a detailed PIC fashion. Electric and magnetic field effects on the charged particles are included in the analysis along with a number of inelastic collision types. A new approach has been considered for including the electric field effects in the particle-based plasma simulations for an ion engine discharge chamber. Our PIC-MCC model is benchmarked on the three-ring NSTAR discharge chamber at the TH-15 operating condition. The numerical results such as currents, particle distributions and thruster performance parameters are both in qualitative and quantitative agreement with experimental results. Numerical results such as single and double xenon ion distributions, primary and secondary electron distributions and particle loss mechanisms inside the discharge chamber obtained from this work will be useful to ion thruster designers to understand and predict the lifetime of discharge components such as the cathode and the cathode-keeper assembly.

Acknowledgments

The authors would like to thank NASA Glenn Research Center and grant monitor Michael Patterson for financially supporting this work under NASA Grant NAG 3-2907. The authors would like to thank Tim Leger for his advice on computational issues and Daniel A. Herman at ASRC Aerospace Corporation for providing experimental data. Also the first author would like to thank the Wright State University Ph.D. program and Tech-X Corporation for their financial support and time allowance, respectively.

References

[1] Arakawa, Y., and Yamada, T., "Monte Carlo Simulations of Primary Electron Motions in Cusped Discharge Chambers," AIAA Paper 90-2654, 1990.

[2] Arakawa, Y., and Ishihara, K., "A Numerical Code for Cusped Ion Thrusters," IEPC Paper 91-118, 1991.

[3] Mahalingam, S., and Menart, J., "Primary Electron Modeling in the Discharge Chamber of an Ion Engine," *38th AIAA/ASME/SAE/ASEE Joint Propulsion Conference*, AIAA Paper 2002-4262, Indianapolis, IN, 2002.

[4] Stueber, T. J., "Ion Thruster Discharge Chamber Simulation in Three Dimension," *41st AIAA/ASME/SAE/ASEE Joint Propulsion Conference*, AIAA Paper 2005-3688, Tucson, AZ, July 2005.

[5] Wirz, R., and Katz, I., "Plasma Processes of DC Ion Thruster Discharge Chambers," *41st AIAA/ASME/SAE/ASEE Joint Propulsion Conference*, AIAA Paper AIAA-2005-3690, Tucson, AZ, July 2005.

[6] Mahalingam, S., and Menart, J. A., "Computational Model Tracking Primary Electrons, Secondary Electrons and Ions in the Discharge Chamber of an Ion Engine," *41st AIAA/ASME/SAE/ASEE Joint Propulsion Conference*, AIAA Paper 2005-4253, Tucson, AZ, 2005.

[7] Mahalingam, S., and Menart, J. A., "Ion Engine Discharge Chamber Plasma Modeling Using a 2-D PIC Simulation," *42nd AIAA/ASME/SAE/ASEE Joint Propulsion Conference*, AIAA Paper 2006-4488, Sacramento, CA, 2006.

[8] Birdsall, C. K., and Langdon, A. B., *Plasma Physics via Computer Simulation*, Adam Hilger, Bristol, England, 1991.

[9] Hockney, R. W., and Eastwood, J. W., *Computer Simulation Using Particles*, 1st edition, Adam Hilger, Bristol, England, 1988.

[10] Taccogna, F., Longo, S., Capitelli, M., and Schneider, R., "Self Similarity in Hall Plasma Discharges: Applications to Particle Models," *Physics of Plasmas*, Vol. 12, No. 053502, 2005, pp. 1–9. doi:10.1063/1.1877517

[11] Mahalingam, S., and Menart, J. A., "Particle Based Plasma Simulations for an Ion Engine Discharge Chamber," AIAA Paper 2007-5247, 2007.

[12] Szabo, J. J., "Fully Kinetic Numerical Modeling of a Plasma Thruster," Ph.D. Dissertation, Massachusetts Institute of Technology, Cambridge, MA, 2001.

[13] Griffiths, D. J., *Introduction to Electrodynamics*, 2nd edition, Prentice Hall, NJ, 1989.

[14] Jameson, K. K., Goebel, D. M., and Watkins, R. M., "Hollow Cathode and Keeper-Region Plasma Measurements," AIAA Paper 2005-3667, 2005.

[15] Raju, G. G., *Gaseous Electronics Theory and Practice*, Taylor and Francis, Boca Raton, FL, 2006.

[16] Strinic, A. I., Malovic, G. N., Petrovic, Z Lj, and Sadeghi, N., "Electron Excitation Coefficients and Cross Sections for Excited Levels of Argon and Xenon Ions," *Plasma Sources Science and Technology* , Vol. 13, No. 2, 2004, pp. 333–342. doi:10.1088/0963-0252/13/2/021

[17] Saloman, E. B., "Energy Levels and Observed Spectral Lines of Xenon, Xe 1 Through Xe 54," *Journal of Physical and Chemical Reference Data*, Vol. 33, No. 3, 2004, pp. 765–921. doi:10.1063/1.1649348

[18] Miller, J. S., Pullins, S. H., Levandier, D. J., Chiu, Y., and Dressler, R. A., "Xenon Charge Exchange Cross Sections for Electrostatic Thruster Models," *Journal of Applied Physics*, Vol. 91, No. 3, 2002, pp. 984–991.
doi:10.1063/1.1426246

[19] Bell, E. W., Djuric, N., and Dunn, G. H., "Electron-Impact Ionization of In+ and Xe+," *Physical Review A*, Vol. 48, No. 6, 1993, pp. 4286–4291.
doi:10.1103/PhysRevA.48.4286

[20] Nedelea, T., and Urbassek, H. M., "Particle-In-Cell Study of Charge-State Segregation in Expanding Plasmas Due to Three-Body Recombination," *Journal of Physics D: Applied Physics*, Vol. 37, No. 21, 2004, pp. 2981–2986.
doi:10.1088/0022-3727/37/21/007

[21] Rejoub, R., Lindsay, B. G., and Stebbings, R. F., "Determination of the Absolute Partial and Total Cross Sections for Electron-Impact Ionization of Rare Gases," *Physical Review A*, Vol. 65, No. 4, 2002, p. 042713.
doi:10.1103/PhysRevA.65.042713

[22] *NIST Atomic Spectra Database*, Ver. 3.1.2, http://physics.nist.gov/PhysRefData/ASD/index.html.

[23] Mahalingam, S., "Particle Based Plasma Simulation for an Ion Engine Discharge Chamber," Ph.D. Dissertation, Wright State University, Dayton, OH, 2007.

[24] Fridman, A., and Kennedy, L. A., *Plasma Physics and Engineering*, Taylor and Francis, New York, 2004.

[25] Seigfried, D. E., and Wilbur, P, J., "A Phenomenological Model Describing Orificed, Hollow Cathode Operation," AIAA Paper 81-0746, April, 1981.

[26] Domonkos, M. T., "Evaluation of Low-Current Orificed Hollow Cathodes," Ph.D. Dissertation, University of Michigan, Ann Arbor, MI, 1999.

[27] Raizer, Y. P., *Gas Discharge Physics*, Springer–Verlag, Berlin, 1991.

[28] *Ansoft Corporation, Maxwell 2D*, http://www.ansoft.com/products/em/maxwell.

[29] Verboncoeur, J. P., Langdon, A. B., and Gladd, N. T., "An Object-Oriented Electromagnetic PIC Code," *Computer Physics Communications*, Vol. 87, Nos. 1–2, 1995, pp. 199–211.
doi:10.1016/0010-4655(94)00173-Y

[30] Bruhwiler, D. L., Giacone, R. E., Cary, J. R., Verboncoeur, J. P., Mardahl, P., Esarey, E., Leemans, W. P., and Shadwick, B, A., "Particle-In-Cell Simulations of Plasma Accelerators and Electron-Neutral Collisions," *Physical Review Special Topics: Accelerators and Beams*, Vol. 4, No. 10, 2001, p. 101302.
doi:10.1103/PhysRevSTAB.4.101302

[31] Birdsall, C. K., "Particle-In-Cell Charged-Particle Simulations, plus Monte Carlo Collisions with Neutral Atoms, PIC-MCC," *IEEE Transactions on Plasma Science*, Vol. 19, No. 2, 1991, pp. 65–85.
doi:10.1109/27.106800

[32] Vahedi, V., and Surendra, M., "A Monte Carlo Collision Model for the Particle-In-Cell Method: Applications to Argon and Oxygen Discharges," *Computer Physics Communications*, Vol. 87, Nos. 1–2, 1995, pp. 179–198.
doi:10.1016/0010-4655(94)00171-W

[33] Verboncoeur, J. P., Parker, G. J., Penetrante, B. M., and Morgan, W. L., "Comparisons of Collision Rates in Particle-In-Cell, Monte Carlo and Boltzmann Codes," *Journal of Applied Physics*, Vol. 80, No. 3, 1996, pp. 1299–1303.
doi:10.1063/1.362929

[34] Mardahl, P., "PIC Code Charge Conservation, Numerical Heating, and Parallelization; Application of XOOPIC to Laser Amplification via Raman Backscatter," Ph.D. Dissertation, University of California, Berkeley, CA, 2001.

[35] Herman, D. A., and Gallimore, D. A., "Discharge Chamber Plasma Structure of a 30-Cm NSTAR-Type Ion Engine," AIAA Paper 2004-3794, 2004.

[36] Mikellides, I. G., Katz, I., Goebel, D. M., and Polk, J. E., "Theoretical Model of a Hollow Cathode Plasma for the Assessment of Insert and Keeper Lifetimes," AIAA Paper 2005-4234, 2005.

[37] Brophy, J. R., Kakuda, R. Y., Polk, J. E., Anderson, J. R., Marcucci, M. G., Brinza, D., Henry, M. D., Fujii, K. K., Mantha, K. R., Stocky J. F., Sovey, J., Patterson, M., Rawlin, V., Hamley, J., Bond, T., Christensen, J., Cardwell, H., Benson, G., Gallagher, J., Matranga, M., and Bushway, D., "Ion Propulsion System (NSTAR) DS1 Technology Validation Report," Jet Propulsion Laboratory, California Inst. of Technology, Rept. 00-10-3A, Pasadena, CA, 2000.

[38] Brophy, J. R., "NASA's Deep Space 1 Ion Engine (Plenary)," *Review of Scientific Instruments*, Vol. 73, No. 2, Feb. 2002, pp. 1071–1078.
doi:10.1063/1.1432470

[39] Brophy, J. R., Brinza, D., Polk, J. E., and Henry, M., "The DS1 Hyper-Extended Mission," AIAA Paper 2002-3673, 2002.

[40] Polk, J. E., Anderson, J. R., Brophy, J. R., Rawlin, V. K., Patterson, M. J., and Sovey, J., "The Effect of Engine Wear on Performance in the NSTAR 8000 Hour Ion Engine Endurance Test," AIAA Paper 97-3387, 1997.

[41] Polk, J. E., Anderson, J. R., Brophy, J. R., Rawlin, V. K., Patterson, M. J., Sovey, J., and Hamley, J., "An Overview of the Results from an 8200 Hour Wear Test of the NSTAR Ion Thruster," AIAA Paper 99-2446, 1999.

[42] Anderson, J. R., Goodfellow, K. D., Polk, J. E., Shotwell, R. F., Rawlin, V. K., Sovey, J. S., and Patterson, M. J., "Results of an On-Going Long Duration Test of the DS1 Flight Spare Engine," AIAA Paper 99-2857, 1999.

[43] Foster, J. E., Soulas, G. C., and Patterson, M. J., "Plume and Discharge Plasma Measurements of an NSTAR-Type Ion Thruster," AIAA Paper 2000-3812, 2000.

[44] Polk, J. E., Kakuda, R. Y., Anderson, J. R., Brophy, J. R., Rawlin, V. K., Patterson, M. J., Sovey, J., and Hamley, J., "Validation of the NSTAR Ion Propulsion System on the Deep Space One Mission: Overview and Initial Research," AIAA Paper 99-2274, 1999.

[45] Brophy, J. R., and Wilbur, P. J., "Simple Performance Model for Ring and Line Cusp Ion Thruster," *AIAA Journal*, Vol. 23, No. 11, 1985, pp. 1731–1736.
doi:10.2514/3.9158

[46] Patterson, M., Haag, T., Rawlin, V., and Kussmaul, M., "NASA 30 Cm Ion Thruster Development Status," AIAA Paper 94-2849, 1994.

[47] Wirz, R., "Discharge Plasma Processes of Ring-Cusp Ion Thrusters," Ph.D. Dissertation, California Institute of Technology, Pasadena, CA, 2005.

[48] Herman, D. A., "The Use of Electrostatic Probes to Characterize the Discharge Plasma Structure and Identify Discharge Cathode Erosion Mechanisms in Ring-Cusp Ion Thrusters," Ph.D. Dissertation, University of Michigan, Ann Arbor, MI, 2005.

[49] Sengupta, A., Goebel, D., Fitzgerald, D., Owens, A., Tynan, G., and Dorner, R., "Experimentally Determined Neutral Density and Plasma Parameters in a 30 Cm Ion Engine," AIAA Paper 2004-3613, 2004.

[50] Sengupta, A., Goebel, D., and Owens, A., "Neutral Density Measurements in an NSTAR Ion Thruster," AIAA Paper 2006-4491, 2006.

[51] Williams, G. J., "The Use of Laser-Induced Fluorescence to Characterize Discharge Cathode Erosion in a 30 Cm Ring-Cusp Ion Thruster," Ph. D. Dissertation, Univ. of Michigan, Ann Arbor, MI, 2000.

[52] Gallimore, A. D., Rovey, J. L., and Herman, D. A., "Erosion Processes of the Discharge Cathode Assembly of Ring-Cusp Gridded Ion Thrusters," *Journal of Propulsion and Power*, Vol. 23, No. 6, Nov.–Dec. 2007, pp. 1271–1278.
doi:10.2514/1.27897

[53] Bennett, W., Ogunjobi, T., and Menart, J. A., "Computational Study of the Effects of Cathode Placement, Electron Energy, and Magnetic Field Strength on the Confinement of Electrons," AIAA Paper 2007-5248, 2007.

[54] Mahalingam, S., and Menart, J. A., "Computational Study of Primary Electron Confinement by Magnetic Fields in the Discharge Chamber of an Ion Engine," *Journal of Propulsion and Power*, Vol. 23, No. 1, 2007, pp. 69–72.
doi:10.2514/1.18366

A. Gallimore
Associate Editor